Enhanced photocatalytic activity of chemically deposited ZnO nanowires using doping and annealing strategies for water remediation

Pierre Gaffuri, Tatjana Dedova, Estelle Appert, Mati Danilson, Adrien Baillard, Odette Chaix-Pluchery, Frank Güell, Ilona Oja-Acik, Vincent Consonni

Enhanced photocatalytic activity of chemically deposited ZnO nanowires using doping and annealing strategies for water remediation

Pierre Gaffuri,[a,b] Tatjana Dedova,[c] Estelle Appert,[a] Mati Danilson,[d] Adrien Baillard,[a] Odette Chaix-Pluchery,[a] Frank Güell,[e] Ilona Oja-Acik,[c] and Vincent Consonni.[a*]

[a] *Université Grenoble Alpes, CNRS, Grenoble INP, LMGP, F-38000 Grenoble, France*

[b] *Université Grenoble Alpes, CNRS, Grenoble INP, Institut NEEL, F-38000 Grenoble, France*

[c] *Laboratory of Thin Film Chemical Technologies, Department of Materials and Environmental Technology, Tallinn Univ. of Technology, Ehitajate tee 5, 19086, Tallinn, Estonia*

[d] *Laboratory of Optoelectronic Materials Physics, Department of Materials and Environmental Technology, Tallinn Univ. of Technology, Ehitajate tee 5, 19086, Tallinn, Estonia*

[e] *ENFOCAT-IN^{2}UB, Universitat de Barcelona, C/Martí i Franquès 1, 08028 Barcelona, Catalunya, Spain*

*Corresponding author: vincent.consonni@grenoble-inp.fr

ABSTRACT

Water pollution represents one of the most challenging ecological threats humankind faces nowadays, resulting in the fast growing development of the heterogeneous photocatalysis using ZnO nanowires. A typical approach to improve the photocatalytic activity consists in achieving their extrinsic doping with group-III elements, but the reasons accounting for the resulting, modified photocatalytic processes are multifactorial and still under debate. In this work, we investigate the effect of the Al and Ga doping of ZnO nanowires grown by chemical bath deposition and of the thermal annealing under oxygen atmosphere on their photocatalytic activity and establish the dependence of the photocatalytic processes on their structural morphology, dimensions, dopant-induced defects, surface properties, and optical absorption and emission. We reveal that the photocatalytic processes strongly depend on the nature of dopants and are systematically

enhanced after thermal annealing. The photocatalytic activity of annealed, Al-doped ZnO nanowires is found to be more efficient, through the direct action of holes besides the efficient action of radicals in the degradation process of organic dyes. These findings show the significance of decoupling the intricate contributions to the photocatalytic activity of ZnO nanowires when the extrinsic doping is used and of thoroughly selecting the nature of dopants.

Keywords: heterogeneous photocatalysis – ZnO nanowires – doping – reaction kinetics – reaction species

1. Introduction

Water pollution is one of the most serious ecological threats humankind faces today. Over the last century, human needs for freshwater were multiplied by a factor of six and they are still increasing significantly owing to the expanding global economy and continuous population growth [1]. However, in the same time, 1.6 billion of people do not have access to freshwater due to poor water management where the demand exceeds the resources [1]. The development of wastewater reclamation and reuse for non-potable and indirect potable purposes has thus received an increasing interest for public institutions [2], but is facing challenges through the systematic presence of persistent organic pollutants (POPs) [3] and trace contaminants including heavy metals [4]. Those are severely harmful to human beings and wildlife due to their carcinogenic nature and poor degradability in the environment, respectively. Even at low concentration (<1mg/L for some dyes), major dyes decrease the water transparency, consume oxygen, and elevate biochemical oxygen demand destroying aquatic life [5]. In the broad family of POPs [3], synthetic organic dyes represent a significant fraction as more than 1,000,000 tons are produced each year as coloring agents in the industries and around 20 % are released in the environment, mainly as textile effluents during the manufacturing process [6]. The removal of organic dyes from wastewater has therefore been considered as a priority and based on various approaches including adsorption, membrane separation, coagulation, and advanced oxidation processes (AOPs) [7, 8]. While the former typically result in the concentration of organic dyes generating a secondary pollution, the latter are known to eliminate organic dyes through a fast, efficient, and non-selective approach. AOPs are based on the *in situ* generation of highly oxidizing agents, like hydroxyl radicals ($^{\bullet}OH$), at room temperature and normal pressure with the assistance of ozone, hydrogen peroxide, Fenton's reagents, ultra-violet light and/or catalysts [7, 8].

Heterogeneous photocatalysis, being considered as one of the most efficient and promising AOPs, was developed following the pioneered work of Fuhishima & Honda in 1972, reporting the splitting of water into hydrogen and oxygen by TiO_2 catalyst when irradiated under UV light [9]. It relies on the formation of electron-hole pairs in direct band gap semiconductors under UV irradiation, hence producing $^{\bullet}OH$ radicals from water molecules and superoxide anion ($^{\bullet}O_2^-$) radicals from O_2 molecules on their surfaces [10, 11].

These radicals are able to efficiently decompose adsorbed organic dyes on their surfaces into CO_2 and harmless organic compounds [10, 11]. Amongst many oxide semiconductor photo-catalysts [12] including TiO_2 [13], ZnO [14, 15], Cu_2O [16], CeO_2 [17], and Fe_2O_3 [18] to name a few, ZnO has emerged as a very promising candidate in the last decade as it is biocompatible and composed of abundant and low-cost elements. Moreover, the energy position of the bottom of the conduction band minimum and of the top of the valence band maximum with respect to the energy position of the normal hydrogen electrode is favorable for its high photocatalytic activity [14, 15]. Its wide band gap energy of 3.37 eV at room temperature along with its higher absorption coefficient over a broad fraction of the solar spectrum when compared to TiO_2 are of high interest [19]. Eventually, ZnO nanomaterials with a larger surface area including nanoparticles as compared to thin films drastically enhance the photocatalytic activity [20, 21]. Alternatively, ZnO nanowires (NWs) have a higher potential for photocatalysis as compared to nanoparticles [22]. They can be grown by the low-temperature and low-cost chemical bath deposition technique operating in water [23], which is further compatible with the development of green chemistry [24]. Different strategies have been developed to increase the photocatalytic activity of ZnO NWs, such as the formation of type II heterostructures [25] as well as the management of intrinsic defects including vacancies [26] and extrinsic doping [27]. In all cases, the main objective has been to maximize the lifetime of electron-hole pairs photo-generated under UV irradiation to increase the photocatalytic activity operating on the surfaces of ZnO NWs.

The extrinsic doping of ZnO NWs creates additional energy levels in the bandgap that are liable to limit the recombination of photo-generated electron-hole pairs by enhancing their separation, but the resulting traps can also act as recombination centers specifically when their concentration is high [14, 27]. In this way, the cationic dopants substituting for the Zn site lattice are the main doping elements and include Sb [28] and Cu [29] as acceptors and Al [30] and Ga [31] as shallow donors. Transition metals including Fe [32, 33], Ni [34] or Co [35, 36] have also been used to take profit from the different oxidation states of these elements. Saleh *et al.* described the phenomena whereby ZnO nanoparticles are doped with Fe^{3+} and Fe^{2+} in the same time, holes (electrons) are trapped with the transition to Fe^{4+} (Fe^{2+}) [37]. These two oxidation states are less stable and release holes (electrons), going back to Fe^{3+}. Other studies have focused on the effect of rare-earth elements such as La [38], Ce [39], and Dy [40] with the idea of benefiting from the specific redox properties of each element, from which the photocatalytic activity of ZnO NWs may be increased. In the vast majority

of reports, the extrinsic doping of ZnO NWs has been found to improve their photocatalytic activity. Nevertheless, the reasons explaining the enhancement that may originate from the effect on the structural morphology (i.e. shape, density), dimensions (i.e. diameter, length), dopant-induced defects, surface properties, and physical properties of ZnO NWs including their optical absorption and electrical conductivity have not been unraveled despite their primary importance and hence are still under debate. Recently, following the pioneered work of Joo et al. aiming at tuning the aspect ratio of ZnO NWs grown by chemical bath deposition (CBD) using the addition of metal cations in the bath [41], the development of the extrinsic doping of ZnO NWs with Al [42, 43] and Ga [44] has thoroughly been achieved. The physicochemical processes at work following the addition of Al nitrate and Ga nitrate in the bath have been studied in detail, along with the CBD conditions required to favor the incorporation of dopants through attractive electrostatic interactions [42-44]. The doping control in ZnO NWs grown by CBD has thus offered recently a greater promise to precisely determine its effect on the performance of devices, in particular in the field of piezoelectric applications [45]. However, no investigation has been reported so far about the effect of the doping with Al and Ga using the approach in Refs. [42-44] on the optical and surface properties of ZnO NWs grown by CBD as well as on the related photocatalytic processes, opening the way for more carefully understanding the specific role of each dopant on their photocatalytic activity.

In this work, we investigate the effect of the Al and Ga doping of ZnO NWs grown by CBD and thermally annealed under oxygen atmosphere on their photocatalytic activity and decouple the different contributions by thoroughly investigating their structural morphology, dimensions, dopant-induced defects, surface properties, and optical absorption and emission, using field-emission scanning electron microscopy (FESEM), X-ray diffraction (XRD), Raman and photoluminescence (PL) spectroscopy, X-ray photoelectron spectroscopy (XPS), UV-visible absorption, and contact angle (CA) measurements. The photocatalytic activity of annealed Al-doped ZnO NWs is found to be much larger and stable in time, through the direct action of holes enhanced by the efficient light trapping in the array in addition to the significant action of radicals in the degradation process of three different organic dyes. The present study enables us to report a comprehensive diagram accounting for the precise effect of each Al and Ga dopant as well as of the thermal annealing on the photocatalytic activity of ZnO NWs.

2. Experimental

2.1 Deposition techniques

ZnO NW arrays were grown by chemical bath deposition on a *c*-axis oriented polycrystalline ZnO seed layer pre-deposited by dip coating on a cleaned (3 × 0.9 cm^2) 150 nm-thick ITO / borosilicate glass substrate (Delta Technology LTD) using a double-step process. The sol-gel process using dip coating and leading to the growth of a 40 nm-thick polycrystalline seed layer composed of well crystallized *c*-axis oriented ZnO nanoparticles is described in Ref. [46]. The growth of vertically-aligned undoped, Ga-doped, and Al-doped ZnO NWs was performed by CBD as described in Refs. [42, 44, 47]. The chemical precursor solution consisted of the standard equimolar (30 mmol/L) mix of zinc nitrate hexahydrate ($Zn(NO_3)_2 \cdot 6H_2O$, Sigma-Aldrich) and HMTA ($C_6H_{12}N_4$, Sigma-Aldrich) in deionized water. To grow Ga- and Al-doped ZnO NWs, gallium nitrate hydrate ($Ga(NO_3)_3 \cdot xH_2O$, Sigma-Aldrich) and aluminium nitrate nonahydrate ($Al(NO_3)_3 \cdot 9H_2O$, Sigma-Aldrich) were, respectively, incorporated into the chemical precursor solution with a concentration of 0.6 mmol/L corresponding to a dopant to zinc precursor ratio of 2 %. In order to favor the incorporation of Al and Ga into the crystal lattice of ZnO NWs, the pH of the solution was set to 10.9 by the addition of ammonia (NH_3, VWR Chemicals) to the chemical precursor solution prior to the deposition start. The CBD of ZnO NWs took place in a sealed glass reactor containing the chemical precursor solution that was further put in an oven kept for 3 hours at 90 °C. Eventually, undoped, Ga-doped and Al-doped ZnO NW arrays were annealed for 1 h at 400 °C under oxygen atmosphere using a dedicated tubular furnace.

2.2 Characterization techniques

The morphology of ZnO NWs was investigated by top-view and cross-sectional view FESEM images using a FEI Quanta 250 FEG-SEM operating at 20 keV. XRD patterns were collected with a Bruker D8 Advance diffractometer using Cu $K\alpha_1$ radiation according to the Bragg−Brentano configuration. Raman scattering spectra were recorded using a Horiba/Jobin Yvon Labram spectrometer equipped with a liquid-nitrogen-cooled CCD detector. The 488 nm excitation line of an Ar^+ laser was used with a power on the sample surface lower than 0.9 mW. The laser beam was focused to a spot size of 1 μm^2 using a 100 times objective. The spectra were calibrated in wavenumber at room temperature by using a silicon reference sample and considering that the theoretical position of the silicon Raman line is set to 520.7 cm^{-1}. XPS measurements

were performed with a Kratos Analytical AXIS ULTRA DLD spectrometer (Manchester, England) in conjunction with a 165-mm hemispherical electron energy analyzer (Kratos Analytical, Manchester, England) and delay-line detector (Kratos Analytical, Manchester, England) to investigate the chemical composition of the surface of ZnO NWs. The analysis was carried out using a monochromatic Al Kα radiation (1486.6 eV) operating at 15 kV and 150 W.

The optical properties of ZnO NW array samples, including total transmittance, total reflectance, and diffuse transmittance, were recorded using a JASCO V-670 UV–Vis–NIR spectrophotometer equipped with an integrating sphere. The optical spectra were recorded in the wavelength range of 330–850 nm and used to calculate the optical bandgap energy (E_g) and the Haze factor as defined by the ratio of the diffuse transmittance over the total transmittance. E_g was calculated from the intercept of the linear portion of $(\alpha h\nu)^2$ vs. $h\nu$ graph with the $h\nu$-axis [48]. Room-temperature PL measurements were made using a chopped Kimmon IK Series He-Cd laser (325 nm and 40 mW). Fluorescence was dispersed with an Oriel Corner Stone 1/8 74000 monochromator, detected using a Hamamatsu H8259-02 with a socket assembly E717-500 photomultiplier, and amplified through a Stanford Research Systems SR830 DSP. A filter in 360 nm was used to stray light. All spectra were corrected for the response function of the setups.

2.3 Photocatalytic measurements

The photocatalytic activity under near UV illumination of ZnO NW arrays was estimated by following the degradation - i.e. the change in concentration with time - of three different organic dyes including methyl orange (MO), methylene blue (MB), and Rhodamine B (RhB). The organic dye concentrations were monitored every 30 minutes using the JASCO V-670 UV-VIS-NIR spectrophotometer. Prior to the photocatalytic activity measurements, the ZnO NW array samples were put in the dark for one hour into the organic dye solution to reach the equilibrium in the adsorption process. A Philips Mercury lamp (two 15 W lamps, model TL-D, λ_{max} = 365 nm) was used as a UV source. The ZnO NW array samples were mounted in a 5 ml UV-cuvette and filled up with 4 ml of organic dye solution. The initial concentration of the organic dye solution was set to 15 mg/L (15 ppm). The measurement of the MO dye concentration took place at a wavelength of 464 nm, MB at 660 nm and RhB at 554 nm. The surface wettability of ZnO NW arrays was investigated by measuring the static water CA on a DSA 25 KRÜSS instrument at room temperature from

three random places on a film surface. CA values were calculated using the sessile drop fitting method. The ZnO NW array samples were cleaned under UV-C irradiation (20 W, λ_{max} = 254 nm) before wettability test and before each photocatalytic activity test using a UV ozone cleaning system (NanoBioAnalytics, UVC-1014). To identify the reactive species actively taken part in the photocatalytic degradation process, one hour long photocatalytic measurements mounting the ZnO NW array samples in the MO solution containing different scavengers were performed. Tert-butanol was used to scavenge hydroxyl radicals ($^{\bullet}OH$), p-benzoquinone to detect the superoxide anion radicals ($^{\bullet}O^{2-}$), and ammonium oxalate to scavenge the holes (h^{+}). The scavenger concentration was set to 1 mmol/L. Finally, the stability of the photocatalytic activity of ZnO NW array was assessed by measuring six repetitive cycles of the MO degradation, each cycle lasting for 3 hours. The repetitive photocatalytic activity test experiments were recorded using the ZnO NW arrays that had undergone the dye degradation and scavenging mechanism tests.

3. Results and discussion

3.1 Structural and optical properties of ZnO nanowires

3.1.1 Morphology and structural properties

A group-III dopant to zinc chemical precursor concentration ratio (i.e. $[Ga(NO_3)_3]/[Zn(NO_3)_2]$ and $[Al(NO_3)_3]/[Zn(NO_3)_2]$) of 2 % was chosen to keep the morphology of ZnO NWs, as shown in **Fig. 1**, while ensuring the proper doping of the nanostructures.

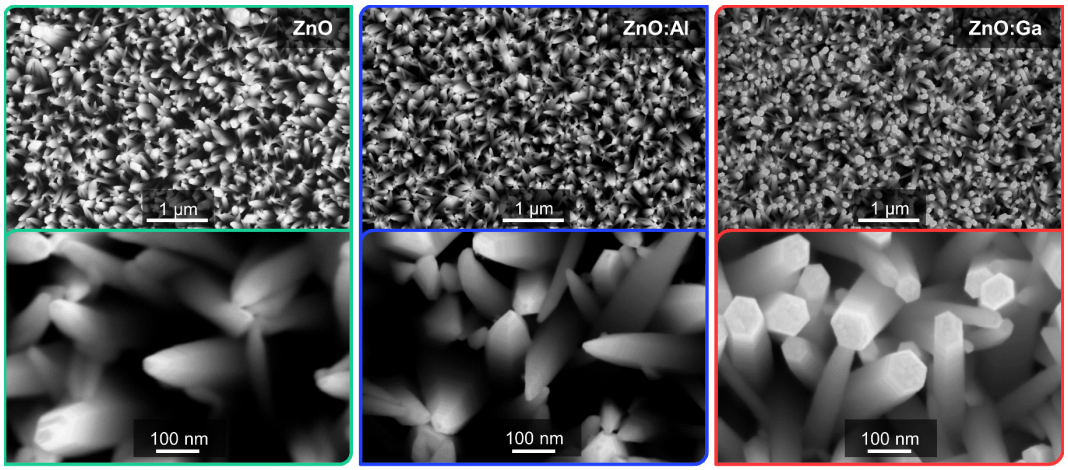

Fig. 1. Top-view FESEM images of as-grown, undoped, Al-doped, and Ga-doped ZnO NW arrays by CBD.

In the case of Al doping, the mean diameter of ZnO NWs is similar to that of the undoped ZnO NWs - i.e. about 60 nm with a needle-like tip, which is in agreement with Ref. [42, 43]. In the case of Ga doping, while the mean diameter of ZnO NWs remains similar, the tip does have a needle-like shape but instead exhibits a flat polar *c*-plane as already reported in Ref. [44]. The length of undoped and Ga-doped ZnO NWs is of the same order and equal to about 6 and 5 µm, respectively, whereas Al-doped ZnO NWs are nearly twice shorter with a length of around 2.5 µm. This drastic decrease in the length of Al-doped ZnO NWs is attributed to a higher supersaturation in the chemical bath from the pH shift to higher values caused by the addition of $Al(NO_3)_3$, in turn favoring the homogeneous growth in the bulk solution at the expense of the heterogeneous growth on the ZnO seed layer [43]. The number density of undoped, Al-doped, and Ga-doped ZnO NWs lies in the same range and equals to about 78, 87, and 76 NWs per μm^2, respectively. The small increase in the density of Al-doped ZnO NWs is again related to the higher supersaturation in the chemical bath, resulting in a higher nucleation rate at the very onset of the growth. The thermal annealing for 1 hour at 400 °C under oxygen atmosphere does not affect the morphology of ZnO NWs, which is stable up to a temperature of around 800 °C as reported in Ref. [49]. From geometrical considerations, the developed surface areas (*S*) of undoped, Al-doped, and Ga-doped ZnO NWs are found to be of about 88, 41, and 71 μm^2 per substrate μm^2. The smaller developed surface area of Al-doped ZnO NWs is mainly due to their shorter length as compared to undoped and Ga-doped ZnO NWs. Beyond the developed surface area value, the surface roughness of ZnO NWs needs to be taken into account for photocatalytic applications. The formation of crystallographic steps induced by the high axial growth rate at that high pH value [42] and possible erosion phenomena from HO^- ions [50] occurs on the nonpolar *m*-plane sidewalls of needle-shaped undoped and Al-doped ZnO NWs. In contrast, the presence of Ga in subsurface stabilizes the nonpolar *m*-planes of Ga-doped ZnO NWs [51, 52], exhibiting much fewer crystallographic steps on their sidewalls.

The effect of the Al and Ga doping as well as of the thermal annealing on the microstructure, phase, and chemical composition of the bulk of ZnO NWs was assessed by XRD and Raman spectroscopy measurements. The XRD patterns of undoped, Al-doped, and Ga-doped ZnO NW arrays before and after thermal annealing are presented in **Fig. 2a**.

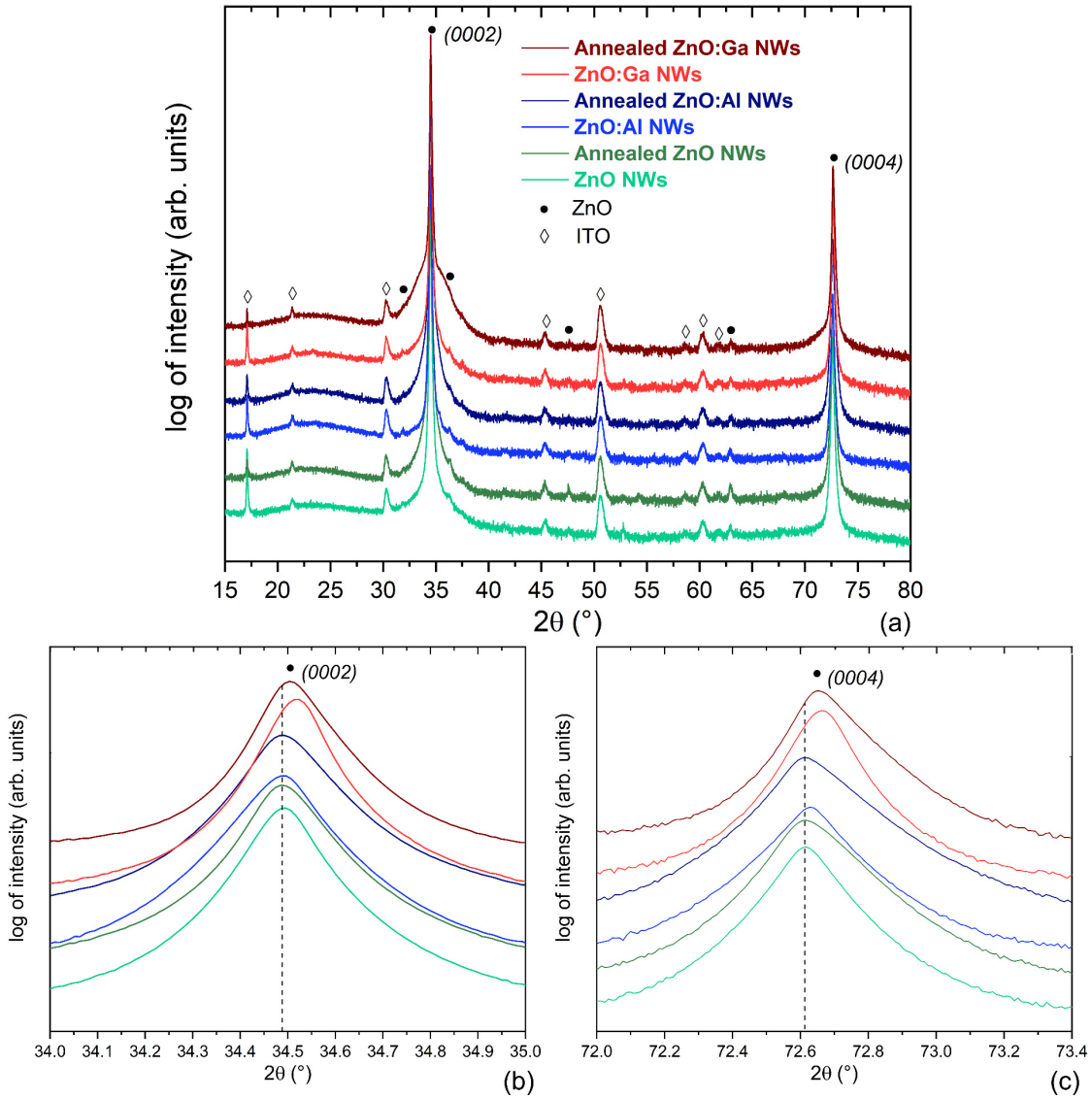

Fig. 2. (a) XRD patterns of undoped, Al-doped, and Ga-doped ZnO NWs, before and after thermal annealing for 1 h at 400 °C under oxygen atmosphere. (b)-(c) Zoom-in in the area of interest around the (0002) and (0004) diffraction peaks of ZnO, respectively.

ZnO NWs crystallize into the wurtzite structure and are preferentially oriented along the polar *c*-axis as indicated by the prominent (0002) and (0004) diffraction peaks at 34.42 and 72.56°, respectively [53]. Additional $(10\bar{1}0)$, $(10\bar{1}1)$, $(10\bar{1}2)$, and $(10\bar{1}3)$ diffraction peaks at around 31.8, 36.2, 47.6 and 62.9° with much weaker intensities originate from the *c*-axis-oriented polycrystalline ZnO seed layer, where some grains exhibit non-polar or semipolar orientations [46]. Further diffraction peaks, as marked with rhombs in **Fig. 2a**, correspond to the ITO layer crystallizing into the bixbyite structure. It is worth mentioning that no Al or Ga containing phases (oxides, hydroxydes, or oxy-hydroxydes) are detected in the XRD patterns, excluding the formation of a residual phase containing the dopants [42, 44]. More importantly, no shift of the

(0002) and (0004) diffraction peaks arises from as-grown and annealed undoped ZnO NW arrays, as shown in **Fig. 2b-c**. This indicates that they are completely relaxed following the homoepitaxial process on the polycrystalline ZnO seed layer [53]. In contrast, the Al and Ga doping of ZnO NWs leads to the alterations of the positions of the (0002) and (0004) diffraction peaks. A significant shift of around 0.1° for the (0002) and (0004) diffraction peaks towards higher angles as compared to undoped ZnO NWs is shown in as-grown Ga-doped ZnO NWs. This corresponds to a decrease in the inter-reticular distance between the *c*-planes and reveals the massive incorporation of Ga into the crystal lattice of ZnO. Such a shift is a typical feature of as-grown Ga-doped ZnO NWs, as reported in Refs. [44, 54-56] The thermal annealing of Ga-doped ZnO NW arrays results in a slight reduction of the shift of the (0002) and (0004) diffraction peaks, owing to a relaxation of internal stresses that is likely associated with a change of the nature and concentration of Ga dopant-induced defects [44]. Similarly, a small shift of the (0002) and (0004) diffraction peaks towards higher angles is revealed in as-grown Al-doped ZnO NWs, indicating the significant incorporation of Al into the crystal lattice of ZnO. This shift is even reversed towards lower angles corresponding to an increase in the inter-reticular distance between the *c*-planes in annealed Al-doped ZnO NW arrays, again suggesting a modification of the nature and concentration of Al dopant-induced defects.

The Raman scattering spectra of undoped, Al-doped, and Ga-doped ZnO NW arrays before and after thermal annealing are presented in **Fig. 3a-b**, respectively. The typical phonon modes of the wurtzite structure of ZnO NWs occur at 100 (E_2^{Low}), 438-440 (E_2^{High}), and 574 (A_1(LO) cm^{-1}). A second-order Raman line points are at 333 cm^{-1} (E_2^{High}- E_2^{Low}). No residual phases containing the dopants are revealed either, which is in agreement with the XRD patterns.

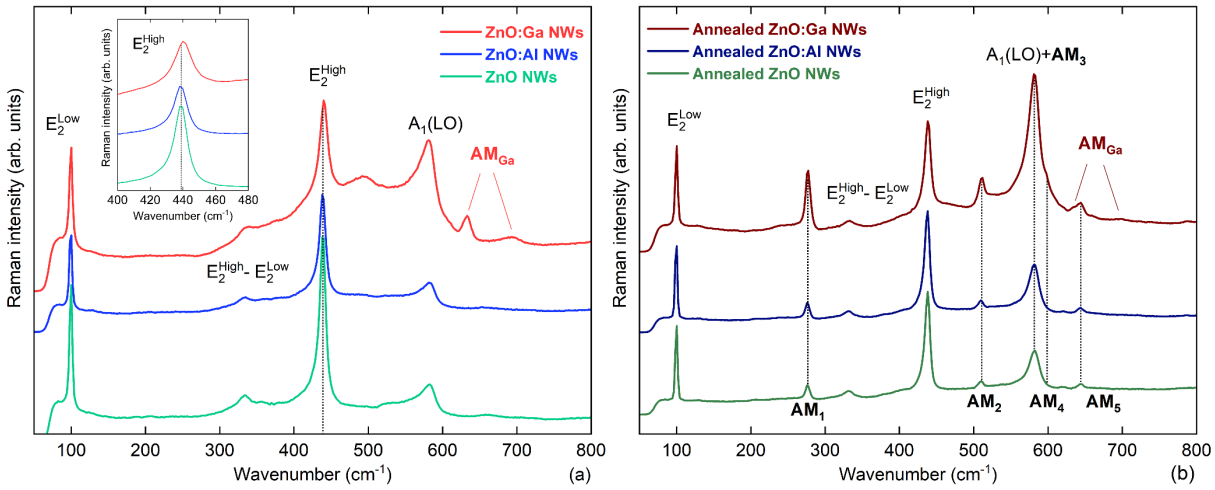

Fig. 3. Raman scattering spectra of undoped, Al-doped, and Ga-doped ZnO NWs (a) before and (b) after thermal annealing for 1 h at 400 °C under oxygen atmosphere. The intensity was normalized to the area under each E_2^{High} line in (b).

Before thermal annealing as presented in **Fig. 3a**, the E_2^{High} line in undoped and Al-doped ZnO NW arrays points at a similar position of 438.0 cm^{-1}, while its full-width-at-half-maximum (FWHM) very slightly increases from 9.6 to 9.7 cm^{-1}, respectively. In contrast, the E_2^{High} line in Ga-doped ZnO NW arrays points at 439.9 cm^{-1} and its FWHM is much larger and of 12.23 cm^{-1}. The intensity of the E_2^{High} line is further greater in as-grown undoped ZnO NW arrays than in doped ZnO NW arrays, revealing a better crystallinity before thermal annealing when no dopants disturbing the crystal lattice are used. Importantly, no additional modes (AM) are shown in undoped and Al-doped ZnO NW arrays. In contrast, two additional modes related to Ga (AM_{Ga}) point at 633.5 and 696.1 cm^{-1} in as-grown Ga-doped ZnO NW arrays. Those so-called AM_{Ga} modes, only observed in Ga-doped ZnO thin films [57-59], nanoparticles [60], and more recently NWs [44], are additional evidence of a massive incorporation of Ga dopants into the crystal lattice.

After thermal annealing as presented in **Fig. 3b**, the E_2^{High} line in undoped, Al-doped, and Ga-doped ZnO NW arrays points at around 438.0 cm^{-1}. Similarly, its FWHM very slightly increases from 8.20 to 8.29 cm^{-1} in undoped and Al-doped ZnO NW arrays, and up to 9.4 cm^{-1} in Ga-doped ZnO NW arrays. Importantly, the classical AMs pointing at around 277 (AM_1), 510 (AM_2), 581 (AM_3), 597 (AM_4), and 643 (AM_5) cm^{-1} in doped ZnO [57] occur in undoped, Al-doped, and Ga-doped ZnO NW arrays. They are typically assigned to the B_1 silent modes in ZnO that are activated by the local breakdown of the translational symmetry coming from the incorporation of dopants [61]. The presence of these AMs in undoped ZnO NW arrays is likely due to the incorporation of residual impurities coming from the chemical precursors used for the CBD process. After a normalization of the Raman spectra to the areas under the E_2^{High} lines, it turns out that the area under the AM lines relative to those in undoped ZnO NW arrays increases by 10 % in Al-doped ZnO NW arrays, and by 372 % in Ga-doped ZnO NW arrays. This confirms the significant and massive incorporations of Al and Ga dopants, respectively, into the crystal lattice of ZnO NWs. The incorporation of Ga dopants into ZnO NWs is however larger than the incorporation of Al dopants, as already reported in ZnO thin films grown by CBD [62]. Correlatively, the position of the AM lines is overall shifted by about 2 cm^{-1} towards higher wavenumbers in Ga-doped ZnO NW arrays.

Eventually, both XRD and Raman scattering measurements demonstrate the high crystalline quality of ZnO NWs, regardless of the nature of extrinsic doping before and after thermal annealing. In the case of the intentional doping, Al and Ga dopants have significantly been incorporated into the crystal lattice.

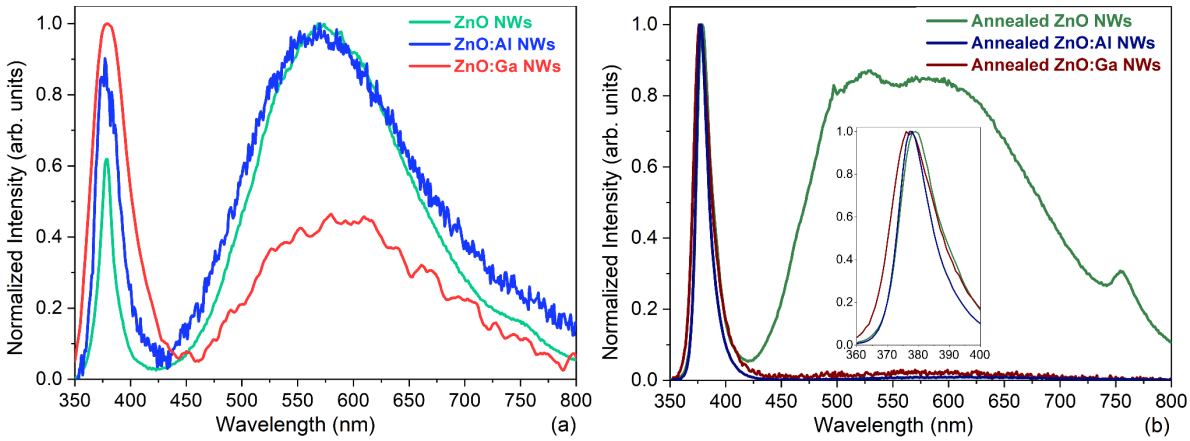

Fig. 4. Room temperature PL spectra of undoped, Al-doped, and Ga-doped ZnO NWs (a) before and (b) after thermal annealing for 1 h at 400 °C under oxygen atmosphere. The intensity was normalized to the highest value. The insert represents the zoom-in in the NBE emission.

3.1.2 Spectroscopic properties

In order to proceed with the identification of dopant-induced defects, room temperature PL spectra of undoped, Al-doped and Ga-doped ZnO NWs are presented in **Fig. 4**. The near-band-edge (NBE) emission of undoped ZnO NWs is centered around 378 nm (i.e. 3.280 eV) and dominated by radiative transitions involving donor-bound A-excitons that include the hydrogen-related defects such as interstitial hydrogen in bond centered sites (H_{BC}), zinc vacancy-hydrogen defect complexes (V_{Zn}-3H), and hydrogen substituting for the O lattice sites (H_O) through the I_4 labeled line [63]. The high concentration of hydrogen-related defects acting as shallow donors is due to the crystallization of ZnO NWs involving a dehydration process of $[Zn(H_2O)_6]^{2+}$ and accounts for the high free electron density of undoped ZnO NWs [63, 64]. The NBE emission of Al-doped and Ga-doped ZnO NWs is centered at 377.5 nm (i.e. 3.285 eV) and 379 nm (i.e. 3.270 eV), respectively, which is attributed to radiative transitions involving donor-bound A excitons that include Al and Ga substituting for the Zn lattice sites (Al_{Zn} and Ga_{Zn}) through the respective I_6 and I_8 labeled lines [65]. The high concentration of Al_{Zn} and Ga_{Zn} shallow donors due to their low formation energy [66, 67] certainly explains their even higher free electron density as reported in Ref. [45]. However, a significant part of Al dopants is expected to lie on the interstitial sites [68]. The visible defect band of undoped, Al-

doped, and Ga-doped ZnO NWs is centered at around 570 nm (i.e. 2.17 eV), 574 nm (i.e. 2.16 eV), and 588 nm (i.e. 2.11 eV), and is typically attributed to hydrogen-related defect complexes [63] that can even include Al and Ga dopants [69]. The role of oxygen vacancies (V_O) in luminescence spectroscopy has been ruled out by density-functional theory calculations, showing that the related luminescence peaks lie in an energy range lower than 1 eV [70]. Interestingly, the relative intensity of the NBE emission over the visible defect band increases when ZnO NWs are doped with Al dopants and even more significantly with Ga dopants. Following the thermal annealing under oxygen atmosphere, undoped, Al-doped, and Ga-doped ZnO NWs exhibit a more intense NBE emission centered at around 378 nm (i.e. 3.28 eV). The visible defect band in annealed, undoped ZnO NWs is still pronounced with two main components at around 529 nm (i.e. 2.34 eV) and 590 nm (i.e. 2.10 eV), although the relative intensity slightly increases showing the relative stability and redistribution of hydrogen-related defects at the annealing temperature of 400 °C [49]. In contrast, the visible defect band in annealed Al-doped and Ga-doped ZnO NWs almost vanishes [71], indicating the drastic decrease in the concentration of hydrogen-related defects that include Al and Ga dopants or not.

3.1.3 Optical absorption properties

To characterize the optical absorption properties of undoped, Al-doped, and Ga-doped ZnO NW arrays, the total transmittance and reflectance along with the diffuse transmittance in the wavelength region of 350-850 nm were recorded by UV-visible spectrophotometry. Haze factors values showing their scattering ability were further calculated as the ratio of the diffuse transmittance over the total transmittance. The total transmittance, reflectance and Haze factor curves versus wavelength are presented in **Fig. 5a** and **b**, respectively.

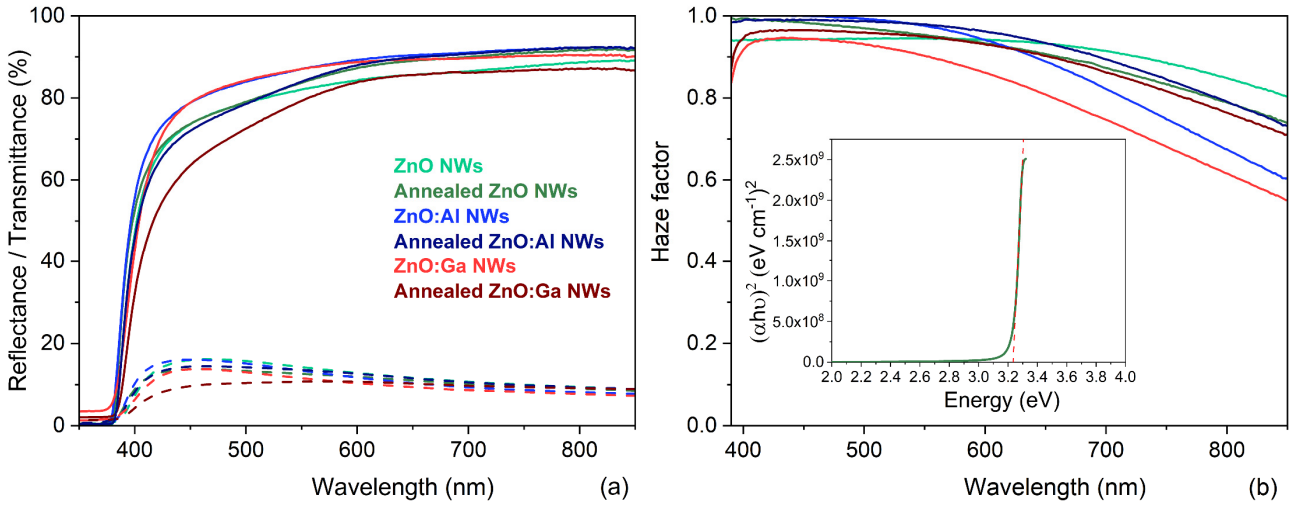

Fig. 5. (a) Total transmittance (solid lines) and reflectance (dashed lines) spectra and (b) Haze factor of undoped, Al-doped, and Ga-doped ZnO NWs before and after thermal annealing for 1 h at 400 °C under oxygen atmosphere. The inset represents the Tauc plot of annealed, doped ZnO NWs, where the red dashed line denotes the fit of the linear portion to deduce the optical band gap energy from its intercept with the *hν*-axis.

All of the ZnO NWs before and after thermal annealing exhibit a fairly similar total transmittance and reflectance with an average value of ~ 85 % and ~12 % in the wavelength region of 550–850 nm, respectively, regardless of the nature of the chemical dopants including Al and Ga. In contrast, the total transmittance more significantly varies in the wavelength region of 450–500 nm. The total transmittance of doped ZnO NWs in the wavelength region of 450–500 nm slightly decreases after thermal annealing being ~13 % lower for annealed Ga-doped ZnO NWs and 6 % lower for annealed Al-doped ZnO NWs as compared to their as-grown counterparts. It is worth noticing that the overall Haze factor values systematically increase after thermal annealing for all of the ZnO NWs. The as-grown Ga-doped ZnO NWs exhibit the lowest Haze factor values as compared to undoped and Al-doped ZnO NWs, which further decrease gradually as the wavelength is increased from 500 nm. This indicates their weaker ability to scatter or preserve the light within the NW arrays. The 95 % value of Haze factor at the wavelength of 450 nm indicates that major scattering processes occurs due to fine structures in the arrays. It gradually decreases as the wavelength is increased, indicating the lowering of scattering processes from large-sized features, e.g. rods. The Al-doped ZnO NW arrays exhibit the highest scattering ability among all of the ZnO NWs, through a laminar Haze factor curve over the studied wavelength region. This indicates that fine structures

and large-sized features are evenly contributed to the scattering process of Al-doped ZnO NW arrays. Those fine structures might be related to the needle shape of Al-doped ZnO NWs with further crystallographic steps, as shown by FESEM imaging in **Fig. 1**. The values of the optical band gap energy (E_g) were calculated from the Tauc plot of $(ahv)^2$ versus hv as shown in Ref. [48]: $\alpha hv = A(hv - E_g)^n$, where hv is the photon energy, α is the absorption coefficient, and A is a constant. For direct band gap semiconductors including ZnO, n = 1/2. As an example, the Tauc plot of annealed, undoped ZnO NWs is presented in the inset of **Fig. 5b**. The E_g values of undoped and Al-doped ZnO NWs before and after thermal annealing lie in the range of 3.21-3.25 eV, which is in agreement with the typical values ranging from 3.24 to 3.30 eV reported for ZnO thin films [48] and nanorods [72]. In contrast, the E_g values of Ga-doped ZnO NWs before and after thermal annealing decreases below 3.20 eV owing to the doping-induced band gap renormalization effect [73], and hence their optical behavior markedly differs.

3.2 Photocatalytic properties and surface composition of ZnO nanowires

3.2.1 Photocatalytic activity

The photocatalytic activity of undoped, Al-doped, and Ga-doped ZnO NW arrays before and after thermal annealing as measured under UV-A irradiation with a 30 W Hg lamp is presented in **Fig. 6** through the evolution of the residual over initial concentration ratios of MO, MB, and RhB organic dyes as a function of time along with the photocatalytic degradation kinetics plots. When no ZnO NW-based photocatalysts are used, the residual over initial concentration ratios are around 100 %, indicating that no significant photocatalytic activity occurs. In contrast, the introduction of ZnO NW-based photocatalysts results in a drastic decrease in the residual over initial concentration ratios of all the organic dyes and hence in a strong improvement of the photocatalytic activity. The photocatalytic degradation kinetics was analyzed within the Langmuir-Hinshelwood model typically used when the initial concentration of organic dyes is sufficiently low as follows [74, 75]:

$$\ln\left(\frac{C_0}{C}\right) = k_S t \quad (1)$$

where k_S is the apparent reaction rate constant, C_0 is the initial concentration of organic dyes, and C is the concentration of organic dyes at reaction time of t, respectively. All the plots of $\ln(C_0/C)$ vs t follow a linear

relationship with a high correlation coefficient (R^2), showing that the photocatalytic degradation of organic dyes by ZnO NWs obeys the pseudo first-order reaction kinetics. The slope deduced from each fit provides an estimate of k_S, as presented in **Table 1**.

First, it is worth noticing that most of ZnO NWs exhibit a photocatalytic activity that is larger to degrade the MB and RhB organic dyes than to degrade the MO organic dye. This may be due to the fact that the adsorption of organic dyes on the surfaces of ZnO NWs depends on the pH value of the solution lying here in the intermediate range (~5.4). In particular, the anionic MO organic dye latter is known to more efficiently adsorb on the surfaces of ZnO NWs at a lower pH value favoring attractive electrostatic interactions [76].

Second, the thermal annealing results in a significant improvement of the photocatalytic activity of all of the annealed ZnO NWs as compared to their as-grown counterparts, regardless of the chemical nature of dopants and of the nature of organic dyes. For example, the photocatalytic activity of undoped ZnO NWs increases by a factor of 1.6 after thermal annealing: the annealed, undoped ZnO NWs have a photocatalytic activity of 58 % for 3h in MO dye solution, whereas the as-grown, undoped ZnO NWs exhibit a photocatalytic activity of only 37 %. The thermal annealing of doped ZnO NWs even shows a more pronounced increase in the photocatalytic activity. For example, the photocatalytic activity of Ga-doped ZnO NWs increases by a factor of 2.7 after thermal annealing: the annealed, Ga-doped ZnO NWs have a photocatalytic activity of 19 % for 3h in MO dye solution, while the as-grown, Ga-doped ZnO NWs exhibit a photocatalytic activity of only 7 %. The photocatalytic activity of Al-doped ZnO NWs doubles after thermal annealing, showing an increase from 33 to 61 %. Therefore, the thermal annealing makes a large contribution to the photocatalytic activity of all of the ZnO NWs, regardless of the chemical nature of dopants including Al and Ga.

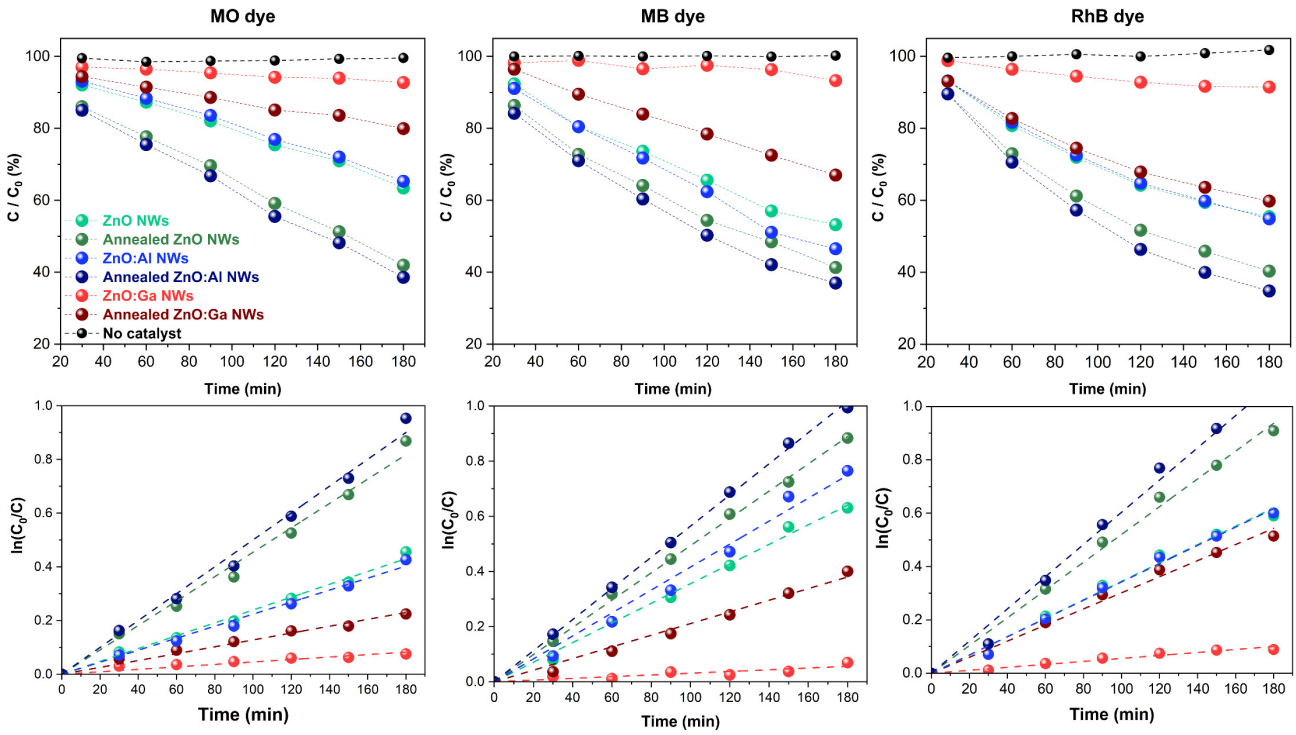

Fig. 6. Evolution of the residual over initial concentration ratios of MO, MB, and RhB organic dyes (top) as a function of time and photocatalytic degradation kinetics plots (bottom), showing the photocatalytic activity under UV-A irradiation with a 30 W Hg lamp of undoped, Al-doped, and Ga-doped ZnO NW arrays before and after thermal annealing for 1h at 400 °C under oxygen atmosphere. The dashed lines in the photocatalytic degradation kinetics plots represent the linear fit from the Langmuir-Hinshelwood model in Eq.(1).

Third, the chemical nature of dopants has a critical effect on the photocatalytic activity of ZnO NWs. The decrease in the residual over initial concentration ratios of all of the organic dyes is much more pronounced in Al-doped ZnO NWs than in Ga-doped ZnO NWs. The record photocatalytic activity of 61, 63, and 65 % for 3h in MO, MB, and RhB dye solutions, respectively, was achieved using annealed, Al-doped ZnO NWs whereas they exhibit the smallest developed surface area of 41 μm^2 per substrate μm^2, namely less than half of the developed surface area of annealed, undoped ZnO NWs that is equal to 88 μm^2 per substrate μm^2. This reveals that the photocatalytic activity of annealed, Al-doped ZnO NWs is much larger than undoped and Ga-doped ZnO NWs before and after thermal annealing. This dependence of the photocatalytic activity on the chemical nature of dopants including Al and Ga is shown regardless of the nature of organic dyes.

3.2.2 Surface composition

In order to understand the differences in the photocatalytic activity, a study of the chemical nature of surfaces in undoped, Al-doped, and Ga-doped ZnO NW arrays before and after thermal annealing was carried out by XPS measurements. The presence of Ga on the surfaces of Ga-doped ZnO NWs is shown in **Fig. S1** through the emission peaks of the Ga $2p_{1/2}$ and $2p_{3/2}$ core levels pointing at 1145 and 1118 eV, respectively [77]. In contrast, the emission peaks related to the Al 2p core levels pointing at around 75 eV in Al-doped ZnO NWs does not occur. This does not indicate the absence of Al on the surfaces of ZnO NWs, as the incorporation of Al dopants is weaker than that of Ga dopants, and this difference has already been reported in ZnO:Al and ZnO:Ga thin films grown by CBD [62]. In view of all the experimental data, we estimate that the amount of Al dopants incorporated into ZnO NWs is much smaller than the amount of Ga dopants incorporated into ZnO NWs [42, 44]. A quantitative analysis gives a Ga to zinc atomic ratio of 1.83 % before thermal annealing, and of 3.07 % after thermal annealing. By comparing that quantification with the approximately 2 % atomic ratio obtained by energy-dispersive X-ray spectroscopy on similar Ga-doped ZnO NWs as reported in Ref. [44], the migration of Ga dopants towards the surfaces of ZnO NWs upon thermal annealing is revealed. This is in good agreement with its presumable stability in the subsurfaces of ZnO [51, 52].

Table 1. Fitting parameters k_S and correlation coefficients R^2 deduced from the photocatalytic degradation kinetics plots using the Langmuir-Hinshelwood model. Note that the developed surface area (S) of ZnO NWs was calculated over a substrate surface area of one μm^2.

	MO		**MB**		**RhB**		**Developped surface area**
	k_S (10^{-3})	R^2	k_S (10^{-3})	R^2	k_S (10^{-3})	R^2	S (μm^2)
ZnO	2.4	0.99	3.6	0.99	3.5	0.99	88
ZnO annealed	4.5	0.99	4.9	0.99	5.2	0.99	88
ZnO:Al	2.2	0.99	4.2	0.99	3.4	0.99	41
ZnO:Al annealed	5.0	0.99	5.7	0.99	6.1	0.99	41
ZnO:Ga	0.5	0.97	0.3	0.93	0.6	0.99	71
ZnO:Ga annealed	1.3	0.99	2.1	0.99	3.0	0.99	71

As regards the nature of surface defects related to zinc and oxygen, the emission peaks attributed to the O 1s and Zn $2p_{3/2}$ core levels are shown in **Fig. 7**.

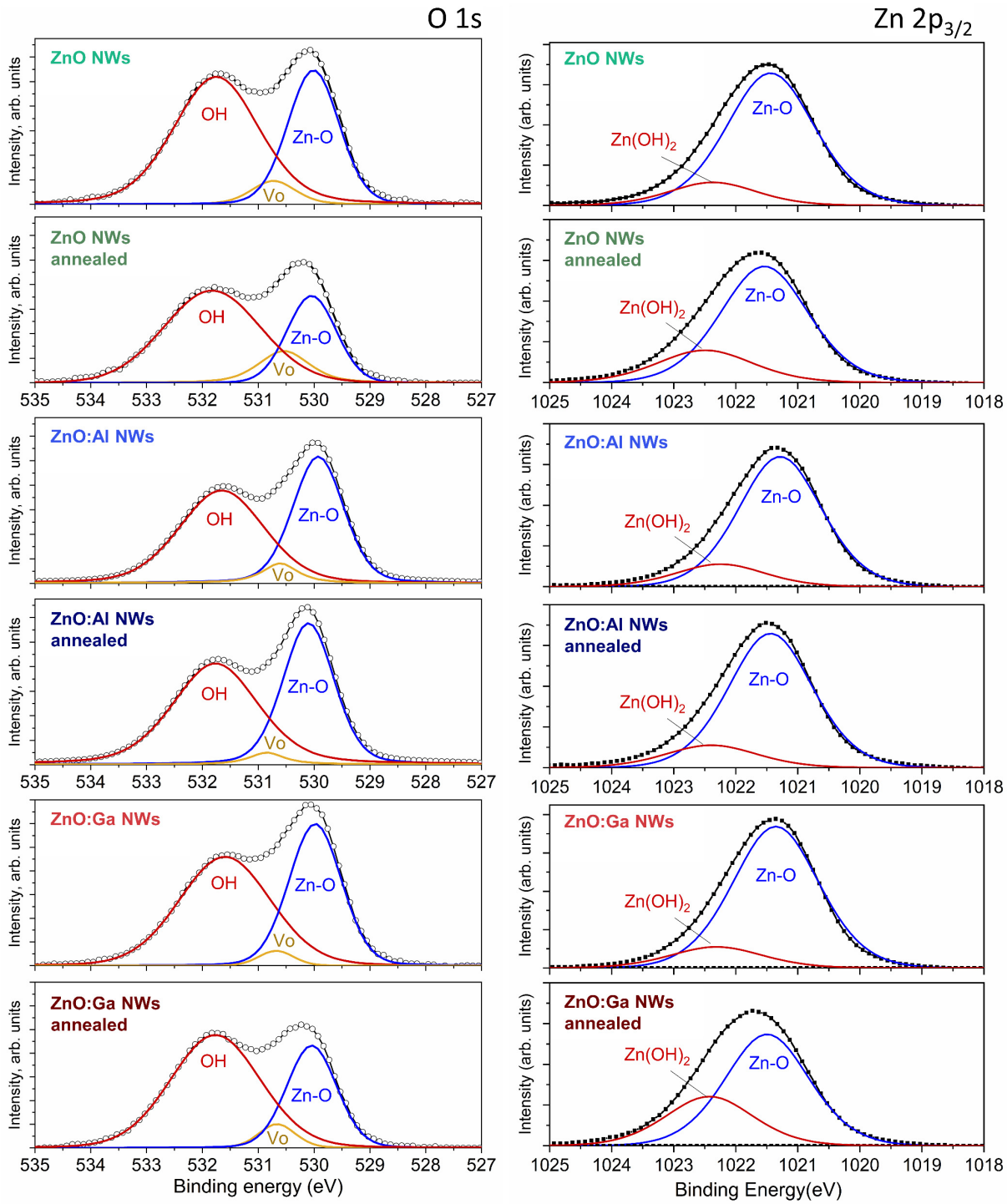

Fig. 7. XPS spectra centered at the emission peaks corresponding to the O 1s and Zn $2p_{3/2}$ core levels of undoped, Al-doped, and Ga-doped ZnO NW arrays, before and after thermal annealing for 1 h at 400 °C under oxygen atmosphere.

The emission peaks assigned to the Zn $2p_{2/3}$ core levels are fairly similar, and asymmetric. These peaks are usually fitted with two Gaussian functions located at 1021.5 eV and 1022.5 eV, corresponding to Zn-O bonds, and $Zn(OH)_2$ groups, respectively [78]. The emission peaks attributed to the O 1s core levels are also

similar to each other. These peaks are usually fitted with three Gaussian functions located at 530 ± 0.1 eV, 531.0 eV, and 532 eV, corresponding to Zn-O bonds [78], V_O [79], and hydroxyl groups (O-H bonds) [80], respectively. The relative ratios of the two/three main components collected on the surfaces of ZnO NWs as calculated from the Zn $2p_{3/2}$/O 1s core levels in XPS spectra, respectively, are presented in **Table 2**. Overall, the emission peak corresponding to the Zn-O bonds systematically shifts towards higher energies following the thermal annealing, which indicates a better crystallinity of annealed ZnO NWs over as-grown ZnO NWs. Conversely, this peak shifts towards lower energies in doped ZnO NWs as compared to their undoped counterparts, again showing the better crystallinity of undoped ZnO NWs.

Table 2. ZnO surface component ratios calculated from the resolved integrated areas of the emission peaks corresponding to the O 1s, Zn $2p_{3/2}$ and C 1s core levels.

	O 1s		**Zn $2p_{3/2}$**
	at%/at%		at%/at%
Samples	V_O/ZnO	OH_{ads}/ZnO	$Zn(OH)_2$/ZnO
ZnO	0.16	0.60	0.17
ZnO annealed	0.40	2.10	0.30
ZnO:Al	0.14	1.45	0.18
ZnO:Al annealed	0.07	1.21	0.18
ZnO:Ga	0.05	1.30	0.16
ZnO:Ga annealed	0.20	2.00	0.46

The contribution of $Zn(OH)_2$ species on the surfaces of all of the ZnO NWs is modest and significantly increases in undoped and Ga-doped ZnO NWs after thermal annealing. In contrast, the contribution of $Zn(OH)_2$ species is fairly constant in Al-doped ZnO NWs after thermal annealing. Correlatively, a significant increase in the contribution of O-H bonds on the surfaces of undoped and Ga-doped ZnO NWs after thermal annealing occurs. For example, the O-H_{ads}/Zn-O ratio in undoped and Ga-doped ZnO NWs increases by a factor of 3.5 and 1.5, from 0.6/1.3 to 2.1/2.0 in as-grown to annealed ZnO NWs, respectively. In contrast, the contribution of O-H bonds on the surfaces of Al-doped ZnO NWs is nearly constant even after thermal annealing. This trend is further supported by wettability measurements, where the CA of all of the ZnO NWs after thermal annealing systematically decreases, before and after an exposition to UV-C irradiation for 10 min as reported in **Table S1** [81]. The enrichment of the surfaces of all of the ZnO NWs by the hydroxyl groups is related to the exo-diffusion of hydrogen in the form of H_{BC} for instance from their bulk upon

thermal annealing [49]. Importantly, the hydroxyl groups are known as some of the main species that contribute to the photocatalytic activity of ZnO NWs through the formation of $^{\bullet}OH$ radicals [81, 82]. In that sense, the higher photocatalytic activity of annealed ZnO NWs as compared to their as-grown counterparts is, to some extent, attributed to the increase in the concentration of hydroxyl groups on their surfaces.

The contribution of V_O on the surfaces of all of the ZnO NWs is fairly weak as compared to the contribution of O-H bonds, suggesting a less than expected impact on their photocatalytic activity [83], and strongly increases in undoped and Ga-doped ZnO NWs after thermal annealing. For instance, the V_O/Zn-O ratio in undoped and Ga-doped ZnO NWs increases by a factor of 2.5 and 4, from 0.16/0.05 to 0.4/0.2 in as-grown to annealed ZnO NWs, respectively. This is likely due to the exo-diffusion of hydrogen in the form of H_O upon thermal annealing, leaving a high concentration of V_O on the surfaces of ZnO NWs [49]. In contrast, the contribution of V_O on the surfaces of Al-doped ZnO NWs after thermal annealing is halved, indicating that the presence of Al dopants modifies the surface chemistry. The interplay between hydroxyl groups and V_O is characteristic of low-temperature solution-grown ZnO nanostructures [81].

Eventually, a weak emission peak related to the C 1s core level is revealed in **Fig. S2**, indicating the minor presence of organic species on the surfaces of all of the ZnO NWs. This probably originates from the adsorption of residues of HMTA molecules on the nonpolar *m*-plane sidewalls of ZnO NWs [47].

3.2.3 Photocatalytic processes and stability

The processes responsible for the photocatalytic activity of undoped, Al-doped, and Ga-doped ZnO NWs before and after thermal annealing were investigated by determining the degradation rate of the MO organic dye using the so-called scavenging technique, as presented in **Fig. 8**. Several selective scavenger solutions were added to the MO organic dye solution to identify the main reactive species. For most of the ZnO NW-based photocatalysts, the degradation rate of the MO organic dye is reduced by the tert-butanol and p-benzoquinone scavengers of radical species (i.e. $^{\bullet}OH$ and $^{\bullet}O_2^-$ radicals, respectively). This reveals that the $^{\bullet}OH$ and $^{\bullet}O_2^-$ radicals represent the main species taking part in the decomposition of the MO organic dye for most of the ZnO NW-based photocatalysts. A notable exception is shown in the case of Ga-doped ZnO NWs before thermal annealing, for which the degradation rate of the MO organic dye is constant even in the presence of the p-benzoquinone scavenger of $^{\bullet}O_2^-$ radicals. This indicates that the only $^{\bullet}OH$ radical species

take part in the decomposition of the MO organic dye, likely explaining the smaller photocatalytic activity of Ga-doped ZnO NWs before thermal annealing. Interestingly, the degradation rate of the MO organic dye is increased by the ammonium oxalate scavenger of holes in undoped and Ga-doped ZnO NWs before and after thermal annealing and is constant in Al-doped ZnO NWs before thermal annealing, indicating that the holes do not significantly contribute to the photocatalytic process in those cases. The increase in the degradation rate induced by the ammonium oxalate scavenger is not due to a variation of pH [76], whose the value of ~5.3 is similar to the MO organic dye solution with no scavenger. In contrast, the degradation rate of the organic MO dye is strongly reduced by the ammonium oxalate scavenger of holes in Al-doped ZnO NWs after thermal annealing. The holes thus take part in the decomposition of the MO organic dye when using Al-doped ZnO NWs after thermal annealing, which accounts for their enhanced photocatalytic activity as compared to their counterpart before thermal annealing.

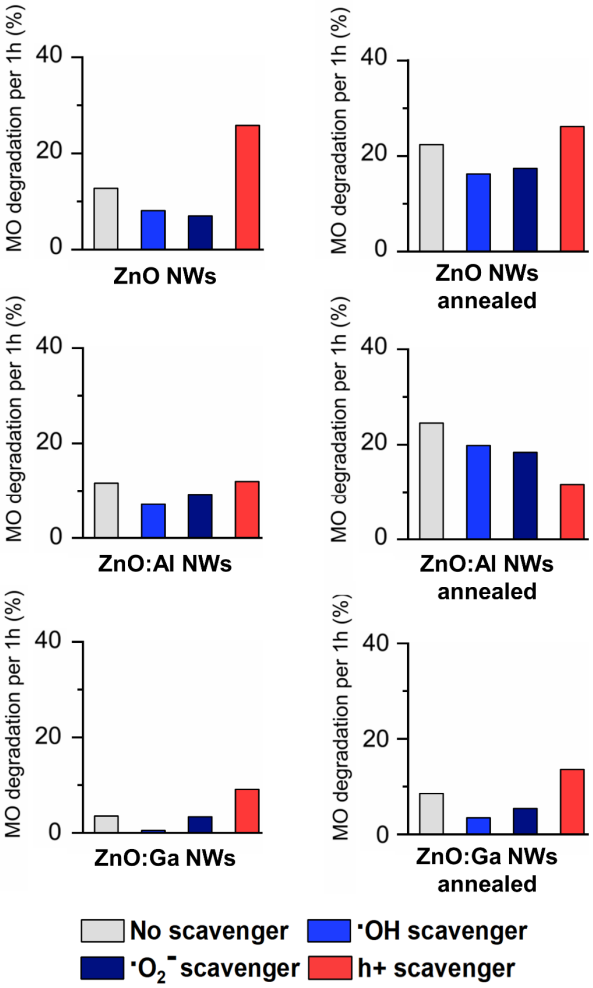

Fig. 8. Degradation rate of the MO organic dye for undoped, Al-doped, and Ga-doped ZnO NWs before and after thermal annealing for 1 h at 400 °C under oxygen atmosphere and in the presence of •OH scavenger (tert-butanol), $^{\bullet}O_2^-$ scavenger (p-benzoquinone), h^+ scavenger (ammonium oxalate).

The stability of the photocatalytic activity of undoped, Al-doped, and Ga-doped ZnO NWs before and after thermal annealing was assessed by measuring the six repetitive cycles of the degradation of the MO organic dye with a 3 h duration for each cycle, as presented in **Fig. 9**. For all of the ZnO NW-based photocatalysts, the stability is excellent before and after thermal annealing, regardless of the chemical nature of dopants including Al and Ga. As the stability tests lasted for 3 h without any measurements in between, the photocatalytic activity is even slightly larger as compared to those measured with an interval of 30 minutes.

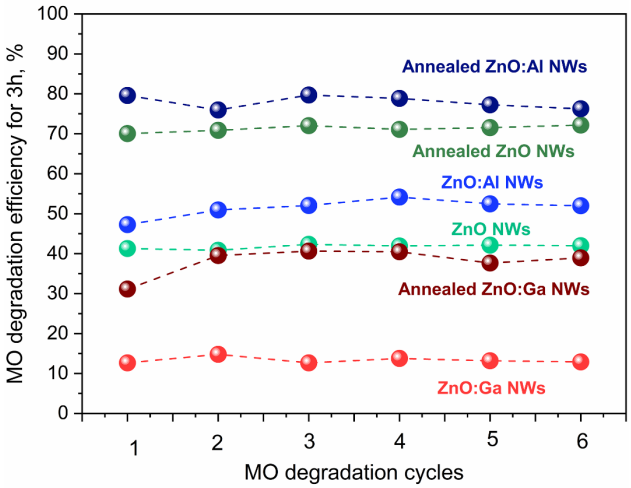

Fig. 9. Evolution of the degradation rate as a function of the MO degradation cycles for undoped, Al-doped, and Ga-doped ZnO NWs before and after thermal annealing for 1 h at 400 °C under oxygen atmosphere.

3.3 Effects of the doping and thermal annealing on the photocatalysis of ZnO nanowires

The whole experimental data reported enable us to make a comprehensive analysis of the effect of the thermal annealing and extrinsic doping with Al and Ga on the photocatalytic properties of ZnO NWs grown by CBD, as recapitulated in **Fig. 10**. It is well-known that the photocatalytic properties of ZnO NWs are dependent upon their morphology driving the developed surface area and the ratio of the nonpolar *m*-plane sidewalls over top polar *c*-faces [84-89], the nature and concentration of intrinsic point defects [26, 83, 85, 87, 89], as well as their ability to trap the light to improve the optical absorption in the UV or visible part of the electromagnetic spectrum to name a few.

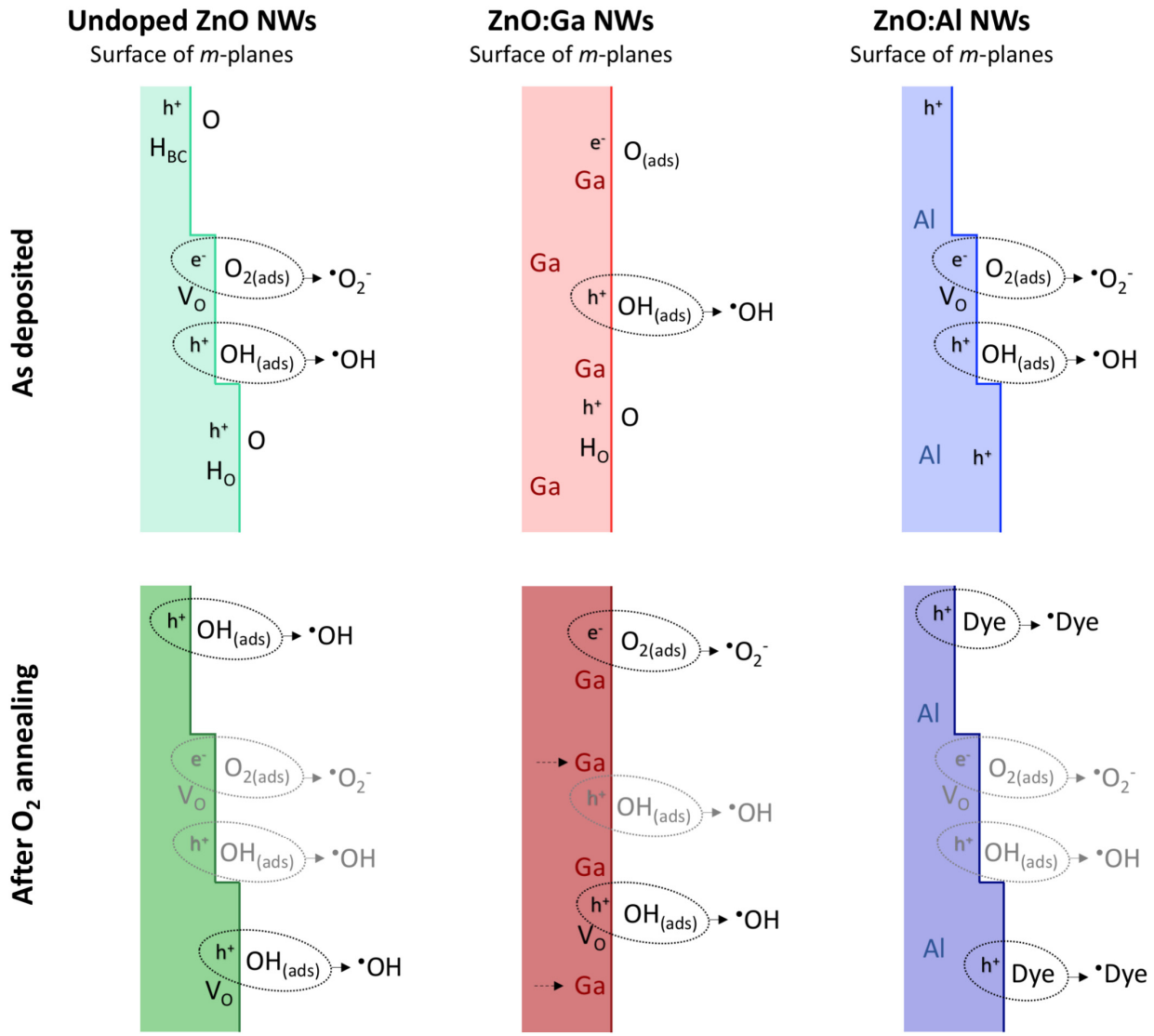

Fig. 10. Schematic diagram summarizing the photocatalytic processes in undoped, Al-doped, and Ga-doped ZnO NWs before and after thermal annealing for 1 h at 400 °C under oxygen atmosphere.

The main chemical reactions generating the reactive species during the photocatalysis of organic dyes by undoped ZnO NWs are summarized as follows [82]:

$$ZnO + \hbar\nu \rightarrow h_{VB}^{+} + e_{CB}^{-} \quad (2)$$

$$h_{VB}^{+} + OH_{(ads)} \rightarrow {}^{\bullet}OH \quad (3)$$

$$h_{VB}^{+} + H_2O \rightarrow {}^{\bullet}OH + H^{+} \quad (4)$$

$$e_{CB}^{-} + O_{2(ads)} \rightarrow {}^{\bullet}O_2^{-} \quad (5)$$

$$Dye + h_{VB}^{+} \rightarrow {}^{\bullet}Dye^{+} \quad (6)$$

Upon UV irradiation with a photon energy higher than the band gap energy, electron-hole pairs are generated in the bulk of undoped ZnO NWs with the holes h_{VB}^+ and electrons e_{CB}^- being in the valence band (VB) and conduction band (CB), respectively (Eq. 2). The free h_{VB}^+ migrate from the bulk towards the surfaces of undoped ZnO NWs owing to the upward band bending related to a surface depletion coming from the adsorbed oxygen anions [90, 91]. As a result, they can readily react with OH groups and H_2O molecules to form $^\bullet$OH radicals (Eqs. 3 and 4). Moreover, the free e_{CB}^- stay in the bulk of undoped ZnO NWs owing to the upward band bending, but some trapped e_{CB}^- on the surfaces of undoped ZnO NWs can efficiently react with O_2 molecules to form $^\bullet O_2^-$ radicals (Eq. 5). The photocatalytic activity of undoped ZnO NWs is thus significant and mostly relies on the contribution of $^\bullet$OH and $^\bullet O_2^-$ radicals as has been shown by the scavenger experiments. Following the thermal annealing under oxygen atmosphere, the enrichment of the surfaces of undoped ZnO NWs with OH groups as has been shown by XPS spectra is activated by the exo-diffusion process of hydrogen-related defects in the form of H_{BC} from their bulk and results in the formation of a higher concentration of $^\bullet$OH radicals. The higher concentration of V_O on the surfaces of annealed, undoped ZnO NWs is also due to the exo-diffusion process of hydrogen-related defects in the form of H_O and leads to the formation of a higher concentration of $^\bullet O_2^-$ radicals. The annealed, undoped ZnO NWs therefore exhibit a higher photocatalytic activity owing to the higher concentration of $^\bullet$OH and $^\bullet O_2^-$ radicals.

In the case of Ga-doped ZnO NWs, the photocatalytic activity before thermal annealing is weak and mostly relies on the contribution of $^\bullet$OH radicals. The surfaces of as-grown Ga-doped ZnO NWs are stabilized by the presence of Ga dopants in the subsurface and hence are smooth, drastically reducing the concentration of V_O such that nearly no $^\bullet O_2^-$ radicals are formed. Following the thermal annealing under oxygen atmosphere, the same exo-diffusion processes of hydrogen-related defects occur, enriching the surfaces of Ga-doped ZnO NWs with OH groups and V_O subsequently resulting in a higher concentration of $^\bullet$OH and $^\bullet O_2^-$ radicals. The photocatalytic activity of annealed, Ga-doped ZnO NWs is thus enhanced drastically, but does not reach the one of undoped ZnO NWs owing their smoother surfaces originating from their enrichment with Ga dopants on the subsurface following the thermal annealing.

In the case of Al-doped ZnO NWs, the photocatalytic activity before thermal annealing is high and relies on the contribution of $^\bullet$OH and $^\bullet O_2^-$ radicals. Given that the Al dopants can occupy both the substitutional Zn site as Al_{Zn} and interstitial sites as Al_i, we expect that they play a more significant role in the incorporation of

hydrogen-related defects with a less concentration, in turn producing a higher concentration of OH groups on the surfaces of ZnO NWs even before thermal annealing. Following the thermal annealing under oxygen atmosphere, the photocatalytic activity of Al-doped ZnO NWs is very high and reaches the best value in the present study. However, the reasons for the present improvement after thermal annealing differs from the explanation given in the cases of undoped and Ga-doped ZnO NWs. Here, the enrichment of the surfaces of annealed, Al-doped ZnO NWs with OH groups does not operate because the reservoir of hydrogen-related defects in the form of H_{BC} is less. A reduction of the concentration of V_O on the surfaces of Al-doped ZnO NWs is even noticed after thermal annealing, which is a typical behavior under oxygen atmosphere. In that sense, the increase in the photocatalytic activity of annealed, Al-doped ZnO NWs is not mostly attributed to the significant modification of the concentration of $^{\bullet}OH$ and $^{\bullet}O_2^-$ radicals. Instead, the enhancement of the photocatalytic activity of annealed, Al-doped ZnO NWs stems from the additional contribution of h_{VB}^+ in the process. A direct oxidation path of the organic dye with the free or trapped h_{VB}^+ on the surfaces of annealed Al-doped ZnO NWs can proceed according to Eq. 6.

Eventually, the needle-shaped morphology of undoped and Al-doped ZnO NWs along with the crystallographic steps on their nonpolar *m*-planes resulting in the formation of polar *c*-planes on the sidewalls enhances their photocatalytic activity as compared to Ga-doped ZnO NWs and hence the degradation of organic dyes for the following reasons: i) the surface area of the active polar *c*-planes is higher in that configuration [84-87], ii) the proximity of the non-polar *m*-planes with the polar *c*-planes on the same sidewalls may form a surface heterojunction separating the photo-generated electron-hole pairs and hence reducing their recombination as reported in TiO_2 nanoparticles [92], iii) the density of surface defects including V_O is higher to activate a higher concentration of $^{\bullet}O_2^-$ radicals [89], iv) the light scattering processes are higher in that configuration as has been shown by transmittance and Haze factor spectra, which may increase the generation rate and amount of electron-hole pairs. Most of these phenomena are expected to lead to the implication of more electron-hole pairs in the photocatalytic processes, which may in turn favor the direct oxidation path using h_{VB}^+ in the case of Al-doped ZnO NWs. The formation of ZnO NWs grown by CBD at high pH using NH_3 is therefore favorable to incorporate the Al dopants, but also to engineer their structural morphology and surfaces, both of them being highly beneficial to boost their photocatalytic activity for water remediation.

4. Conclusion

We have investigated the effect of the extrinsic doping of ZnO NWs grown by CBD using Al and Ga and of the thermal annealing under oxygen atmosphere on their photocatalytic activity to degrade three organic dyes including MO, MB, and RhB. The different contributions to the photocatalytic activity originating from the structural morphology, dimensions, dopant-induced defects, surface properties, and optical absorption of ZnO NWs have been decoupled to cast a light on the dominant photocatalytic processes. We have shown that undoped and doped ZnO NWs exhibit a more efficient photocatalytic activity to degrade the MB and RhB organic dyes than to degrade the MO organic dye and that the photocatalytic processes systematically obey a pseudo-first order reaction kinetic. The photocatalytic activity of as-grown, undoped and Al-doped ZnO NWs involving $^{\bullet}OH$ and $^{\bullet}O_2^-$ radicals with a high concentration is much larger than the photocatalytic activity of Ga-doped ZnO NWs only involving $^{\bullet}OH$ radicals. The thermal annealing under oxygen atmosphere further results in a drastic enhancement of the photocatalytic activity through i) the formation of $^{\bullet}OH$ and $^{\bullet}O_2^-$ radicals with a higher concentration coming from the exo-diffusion process of hydrogen-related defects enriching the surfaces with OH groups and V_O in undoped and Ga-doped ZnO NWs, and i) the activation of the direct oxidation path using h_{VB}^+ in Al-doped ZnO NWs. The needle-shaped morphology of undoped and Al-doped ZnO NWs along with the crystallographic steps on their nonpolar *m*-planes leading to the formation of active polar *c*-planes on the sidewalls additionally play a major role in the improvement of the photocatalytic activity. The annealed, Al-doped ZnO NWs are hence found to exhibit the most efficient photocatalytic activity despite their smallest developed surface area. The present study reports a comprehensive analysis accounting for the precise effect of each Al and Ga dopant as well as of the thermal annealing on the photocatalytic activity of ZnO NWs and shows the interest in working at high pH during the CBD using NH_3. It eventually emphasizes the critical importance to select the dopant with care and the requirement to decouple the intricate contributions to the photocatalytic processes at work in ZnO NWs for water remediation.

Declaration of Competing Interest

The authors declare that they have no known competing financial interests or personal relationships that could have appeared to influence the work reported in this paper.

Acknowledgments

The authors would like to thank Hervé Roussel, Grenoble, France for his assistance in the XRD experiments. P.G. was supported by a doctoral fellowship from the CDP Eco-SESA project (ANR-15-IDEX-02). V.C. gratefully thanks the financial support from the French National Research Agency through the project DOSETTE (ANR-17-CE24-0003). They further acknowledge the facilities, and the scientific and technical assistance of the CMTC characterization platform of Grenoble INP, which is supported by the Centre of Excellence of Multifunctional Architectured Materials (LabEx CEMAM) under the contract ANR-10-LABX-44-01 funded by the "Investments for the Future" Program. Funding by the Carnot Institute Energies du Futur through the project ECOLED is also acknowledged. The authors acknowledge the MAEDI and MENESR French Ministries and the Estonian Research Council for a financial support through the Parrot program (n°42401QH). The study was also funded by the Estonian Research Council project PRG627, the Estonian Centre of Excellence project TK141 (TAR16016EK) “Advanced materials and high-technology devices for energy recuperation systems”, and the European Commission’s H2020 program under the ERA Chair project 5GSOLAR grant agreement No 952509.

Appendix A. Supplementary material

Supplementary data to this article can be found online.

References

[1] United Nations Educational Organization, The United Nations World Water Development Report 2021, United Nations, 2021.
[2] T.W. Hartley, Public perception and participation in water reuse, Desalination 187 (2006) 115-126.
[3] K.C. Jones, P. de Voogt, Persistent organic pollutants (POPs): state of the science, Environ. Pollut. 100 (1999) 209-221.
[4] J. Viers, B. Dupré, J. Gaillardet, Chemical composition of suspended sediments in World Rivers: New insights from a new database, Sci. Total Environ. 407 (2009) 853-868.
[5] F.M.D. Chequer, G.A.R. de Oliveira, E.R.A. Ferraz, J.C. Cardoso, M.V.B. Zanoni, D.P. de Oliveira, Textile Dyes: Dyeing Process and Environmental Impact, 2013.
[6] A. Tkaczyk, K. Mitrowska, A. Posyniak, Synthetic organic dyes as contaminants of the aquatic environment and their implications for ecosystems: A review, Sci. Total Environ. 717 (2020) 137222.
[7] M.A. Oturan, J.-J. Aaron, Advanced Oxidation Processes in Water/Wastewater Treatment: Principles and Applications. A Review, Crit. Rev. Environ. Sci. Tech. 44 (2014) 2577-2641.
[8] M. Salimi, A. Esrafili, M. Gholami, A. Jonidi Jafari, R. Rezaei Kalantary, M. Farzadkia, M. Kermani, H.R. Sobhi, Contaminants of emerging concern: a review of new approach in AOP technologies, Environ. Monit. Assess. 189 (2017) 414.
[9] A. Fujishima, K. Honda, Electrochemical Photolysis of Water at a Semiconductor Electrode, Nature 238 (1972) 37-38.

[10] J.-M. Herrmann, Heterogeneous photocatalysis: fundamentals and applications to the removal of various types of aqueous pollutants, Catal. Today 53 (1999) 115-129.
[11] J.M. Herrmann, Heterogeneous photocatalysis: state of the art and present applications, Top. Catal. 34 (2005) 49-65.
[12] R. Gusain, K. Gupta, P. Joshi, O.P. Khatri, Adsorptive removal and photocatalytic degradation of organic pollutants using metal oxides and their composites: A comprehensive review, Adv. Colloid Interface Sci. 272 (2019) 102009.
[13] F. Han, V.S.R. Kambala, M. Srinivasan, D. Rajarathnam, R. Naidu, Tailored titanium dioxide photocatalysts for the degradation of organic dyes in wastewater treatment: A review, Appl. Catal-A: Gen. 359 (2009) 25-40.
[14] K.M. Lee, C.W. Lai, K.S. Ngai, J.C. Juan, Recent developments of zinc oxide based photocatalyst in water treatment technology: A review, Water Res. 88 (2016) 428-448.
[15] K. Qi, B. Cheng, J. Yu, W. Ho, Review on the improvement of the photocatalytic and antibacterial activities of ZnO, J. Alloys Comp. 727 (2017) 792-820.
[16] A.M. Mohammed, S.S. Mohtar, F. Aziz, S.A. Mhamad, M. Aziz, Review of various strategies to boost the photocatalytic activity of the cuprous oxide-based photocatalyst, J. Environ. Chem. Eng. 9 (2021) 105138.
[17] M. Kurian, Cerium oxide based materials for water treatment – A review, J. Environ. Chem. Eng. 8 (2020) 104439.
[18] C.N.C. Hitam, A.A. Jalil, A review on exploration of Fe_2O_3 photocatalyst towards degradation of dyes and organic contaminants, J. Environ. Manag. 258 (2020) 110050.
[19] S. Sakthivel, B. Neppolian, M.V. Shankar, B. Arabindoo, M. Palanichamy, V. Murugesan, Solar photocatalytic degradation of azo dye: comparison of photocatalytic efficiency of ZnO and TiO_2, Sol. Energy Mater. Sol. Cells 77 (2003) 65-82.
[20] A. Di Mauro, M.E. Fragalà, V. Privitera, G. Impellizzeri, ZnO for application in photocatalysis: From thin films to nanostructures, Mat. Sci. Semicond. Proc. 69 (2017) 44-51.
[21] C.B. Ong, L.Y. Ng, A.W. Mohammad, A review of ZnO nanoparticles as solar photocatalysts: Synthesis, mechanisms and applications, Renew. Sust. Ener. Rev. 81 (2018) 536-551.
[22] S. Baruah, M.A. Mahmood, M.T.Z. Myint, T. Bora, J. Dutta, Enhanced visible light photocatalysis through fast crystallization of zinc oxide nanorods, Beilstein J. Nanotechnol. 1 (2010) 14-20.
[23] L. Vayssieres, K. Keis, S.E. Lindquist, A. Hagfeldt, Purpose-built anisotropic metal oxide material: 3D highly oriented microrod array of ZnO, J. Phys. Chem. B, 105 (2001) 3350-3352.
[24] P. Anastas, N. Eghbali, Green Chemistry: Principles and Practice, Chem. Soc. Rev. 39 (2010) 301-312.
[25] Y. Wang, Q. Wang, X. Zhan, F. Wang, M. Safdar, J. He, Visible light driven type II heterostructures and their enhanced photocatalysis properties: a review, Nanoscale 5 (2013) 8326-8339.
[26] D. Chen, Z. Wang, T. Ren, H. Ding, W. Yao, R. Zong, Y. Zhu, Influence of Defects on the Photocatalytic Activity of ZnO, J. Phys. Chem. C 118 (2014) 15300-15307.
[27] M. Samadi, M. Zirak, A. Naseri, E. Khorashadizade, A.Z. Moshfegh, Recent progress on doped ZnO nanostructures for visible-light photocatalysis, Thin Solid Films 605 (2016) 2-19.
[28] J.M. Wu, C.-W. Fang, L.-T. Lee, H.-H. Yeh, Y.-H. Lin, P.-H. Yeh, L.-N. Tsai, L.-J. Lin, Photoresponsive and Ultraviolet to Visible-Light Range Photocatalytic Properties of ZnO:Sb Nanowires, J. Electrochem. Soc. 158 (2011) K6.
[29] R. Mohan, K. Krishnamoorthy, S.-J. Kim, Enhanced photocatalytic activity of Cu-doped ZnO nanorods, Solid State Commun. 152 (2012) 375-380.
[30] N.R. Khalid, A. Hammad, M.B. Tahir, M. Rafique, T. Iqbal, G. Nabi, M.K. Hussain, Enhanced photocatalytic activity of Al and Fe co-doped ZnO nanorods for methylene blue degradation, Ceram. Int. 45 (2019) 21430-21435.
[31] M.N. Cardoza-Contreras, A. Vásquez-Gallegos, A. Vidal-Limon, J.M. Romo-Herrera, S. Águila, O.E. Contreras, Photocatalytic and Antimicrobial Properties of Ga Doped and Ag Doped ZnO Nanorods for Water Treatment, Catalysts 9 (2019).
[32] Y. Zhang, M.K. Ram, E.K. Stefanakos, D.Y. Goswami, Enhanced photocatalytic activity of iron doped zinc oxide nanowires for water decontamination, Surf. Coat. Technol. 217 (2013) 119-123.
[33] Y.G. Habba, M. Capochichi-Gnambodoe, Y. Leprince-Wang, Enhanced Photocatalytic Activity of Iron-Doped ZnO Nanowires for Water Purification, Appl. Sci. 7 (2017).

[34] I. Loyola Poul Raj, A. Jegatha Christy, R. David Prabu, N. Chidhambaram, M. Shkir, S. AlFaify, A. Khan, Significance of Ni doping on structure-morphology-photoluminescence, optical and photocatalytic activity of CBD grown ZnO nanowires for opto-photocatalyst applications, Inorg. Chem. Commun. 119 (2020) 108082.
[35] A. Šutka, T. Käämbre, R. Pärna, I. Juhnevica, M. Maiorov, U. Joost, V. Kisand, Co doped ZnO nanowires as visible light photocatalysts, Solid State Sci. 56 (2016) 54-62.
[36] W. Li, G. Wang, C. Chen, J. Liao, Z. Li, Enhanced Visible Light Photocatalytic Activity of ZnO Nanowires Doped with Mn^{2+} and Co^{2+} Ions, Nanomaterials 7 (2017) 20.
[37] R. Saleh, N.F. Djaja, UV light photocatalytic degradation of organic dyes with Fe-doped ZnO nanoparticles, Superlattices Microstruct. 74 (2014) 217-233.
[38] T. Jia, W. Wang, F. Long, Z. Fu, H. Wang, Q. Zhang, Fabrication, characterization and photocatalytic activity of La-doped ZnO nanowires, J. Alloys Comp. 484 (2009) 410-415.
[39] O. Yayapao, S. Thongtem, A. Phuruangrat, T. Thongtem, Sonochemical synthesis, photocatalysis and photonic properties of 3% Ce-doped ZnO nanoneedles, Ceram. Int. 39 (2013) S563-S568.
[40] O. Yayapao, T. Thongtem, A. Phuruangrat, S. Thongtem, Sonochemical synthesis of Dy-doped ZnO nanostructures and their photocatalytic properties, J. Alloys Comp. 576 (2013) 72-79.
[41] J. Joo, B.Y. Chow, M. Prakash, E.S. Boyden, J.M. Jacobson, Face-selective electrostatic control of hydrothermal zinc oxide nanowire synthesis, Nat. Mater. 10 (2011) 596-601.
[42] C. Verrier, E. Appert, O. Chaix-Pluchery, L. Rapenne, Q. Rafhay, A. Kaminski-Cachopo, V. Consonni, Effects of the pH on the Formation and Doping Mechanisms of ZnO Nanowires Using Aluminum Nitrate and Ammonia, Inorg. Chem. 56 (2017) 13111-13122.
[43] C. Verrier, E. Appert, O. Chaix-Pluchery, L. Rapenne, Q. Rafhay, A. Kaminski-Cachopo, V. Consonni, Tunable Morphology and Doping of ZnO Nanowires by Chemical Bath Deposition Using Aluminum Nitrate, J. Phys. Chem. C 121 (2017) 3573-3583.
[44] P. Gaffuri, E. Appert, O. Chaix-Pluchery, L. Rapenne, M. Salaun, V. Consonni, The Path of Gallium from Chemical Bath into ZnO Nanowires: Mechanisms of Formation and Incorporation, Inorg. Chem. 58 (2019) 10269-10279.
[45] O. Synhaivskyi, D. Albertini, P. Gaffuri, J.-M. Chauveau, V. Consonni, B. Gautier, G. Bremond, Evidence of Piezoelectric Potential and Screening Effect in Single Highly Doped ZnO:Ga and ZnO:Al Nanowires by Advanced Scanning Probe Microscopy, J. Phys. Chem. C 125 (2021) 15373-15383.
[46] S. Guillemin, E. Appert, H. Roussel, B. Doisneau, R. Parize, T. Boudou, G. Bremond, V. Consonni, Controlling the Structural Properties of Single Step, Dip Coated ZnO Seed Layers for Growing Perfectly Aligned Nanowire Arrays, J. Phys. Chem. C 119 (2015) 21694-21703.
[47] R. Parize, J. Garnier, O. Chaix-Pluchery, C. Verrier, E. Appert, V. Consonni, Effects of Hexamethylenetetramine on the Nucleation and Radial Growth of ZnO Nanowires by Chemical Bath Deposition, J. Phys. Chem. C 120 (2016) 5242-5250.
[48] B.D. Viezbicke, S. Patel, B.E. Davis, D.P. Birnie Iii, Evaluation of the Tauc method for optical absorption edge determination: ZnO thin films as a model system, Phys. Status Sol. B 252 (2015) 1700-1710.
[49] J. Villafuerte, O. Chaix-Pluchery, J. Kioseoglou, F. Donatini, E. Sarigiannidou, J. Pernot, V. Consonni, Engineering nitrogen- and hydrogen-related defects in ZnO nanowires using thermal annealing, Phys. Rev. Mater. 5 (2021) 056001.
[50] M. Willander, L.L. Yang, A. Wadeasa, S.U. Ali, M.H. Asif, Q.X. Zhao, O. Nur, Zinc oxide nanowires: controlled low temperature growth and some electrochemical and optical nano-devices, J. Mater. Chem. 19 (2009) 1006-1018.
[51] J.I. Sohn, W.-K. Hong, S. Lee, S. Lee, J. Ku, Y.J. Park, J. Hong, S. Hwang, K.H. Park, J.H. Warner, S. Cha, J.M. Kim, Surface energy-mediated construction of anisotropic semiconductor wires with selective crystallographic polarity, Sci. Rep. 4 (2014) 5680.
[52] V. Sallet, C. Sartel, S. Hassani, C. Vilar, G. Amiri, A. Lusson, F. Jomard, P. Galtier, I. Lefebvre, C. Delerue, M.K. Hamza, B. Canut, B. Masenelli, Crystal Facet Engineering in Ga-Doped ZnO Nanowires for Mid-Infrared Plasmonics, Cryst. Growth Des. 18 (2018) 4287-4295.
[53] S. Guillemin, V. Consonni, E. Appert, E. Puyoo, L. Rapenne, H. Roussel, Critical Nucleation Effects on the Structural Relationship Between ZnO Seed Layer and Nanowires, J. Phys. Chem. C 116 (2012) 25106-25111.

[54] G.C. Park, S.M. Hwang, J.H. Choi, Y.H. Kwon, H.K. Cho, S.-W. Kim, J.H. Lim, J. Joo, Effects of In or Ga doping on the growth behavior and optical properties of ZnO nanorods fabricated by hydrothermal process, Phys. Status Sol. A, 210 (2013) 1552-1556.
[55] S. Kim, G. Nam, H. Park, H. Yoon, S. H. Lee, J.S. Kim, D.Y. Kim, S.-O. Kim, J. Y. Leem, Effects of Doping with Al, Ga, and In on Structural and Optical Properties of ZnO Nanorods Grown by Hydrothermal Method, Bull. Kor. Chem. Soc. 34 (2013) 1205-1211.
[56] J.H. Lim, S.M. Lee, H.-S. Kim, H.Y. Kim, J. Park, S.-B. Jung, G.C. Park, J. Kim, J. Joo, Synergistic effect of Indium and Gallium co-doping on growth behavior and physical properties of hydrothermally grown ZnO nanorods, Sci. Rep. 7 (2017) 41992.
[57] C. Bundesmann, N. Ashkenov, M. Schubert, D. Spemann, T. Butz, E.M. Kaidashev, M. Lorenz, M. Grundmann, Raman scattering in ZnO thin films doped with Fe, Sb, Al, Ga, and Li, Appl. Phys. Lett. 83 (2003) 1974-1976.
[58] M. Gabás, P. Díaz-Carrasco, F. Agulló-Rueda, P. Herrero, A.R. Landa-Cánovas, J.R. Ramos-Barrado, High quality ZnO and Ga:ZnO thin films grown onto crystalline Si (100) by RF magnetron sputtering, Sol. Energy Mater. Sol. Cells 95 (2011) 2327-2334.
[59] C. Lung, M. Toma, M. Pop, D. Marconi, A. Pop, Characterization of the structural and optical properties of ZnO thin films doped with Ga, Al and (Al+Ga), J. Alloys Comp. 725 (2017) 1238-1243.
[60] G. Pineda-Hernández, A. Escobedo-Morales, U. Pal, E. Chigo-Anota, Morphology evolution of hydrothermally grown ZnO nanostructures on gallium doping and their defect structures, Mater. Chem. Phys. 135 (2012) 810-817.
[61] F.J. Manjón, B. Marí, J. Serrano, A.H. Romero, Silent Raman modes in zinc oxide and related nitrides, J. Appl. Phys. 97 (2005) 053516.
[62] S. Edinger, N. Bansal, M. Bauch, R.A. Wibowo, R. Hamid, G. Trimmel, T. Dimopoulos, Comparison of chemical bath-deposited ZnO films doped with Al, Ga and In, J. Mater. Sci. 52 (2017) 9410-9423.
[63] J. Villafuerte, F. Donatini, J. Kioseoglou, E. Sarigiannidou, O. Chaix-Pluchery, J. Pernot, V. Consonni, Zinc Vacancy–Hydrogen Complexes as Major Defects in ZnO Nanowires Grown by Chemical Bath Deposition, J. Phys. Chem. C 124 (2020) 16652-16662.
[64] C. Lausecker, B. Salem, X. Baillin, V. Consonni, Modeling the Elongation of Nanowires Grown by Chemical Bath Deposition Using a Predictive Approach, J. Phys. Chem. C 123 (2019) 29476-29483.
[65] B.K. Meyer, J. Sann, S. Eisermann, S. Lautenschlaeger, M.R. Wagner, M. Kaiser, G. Callsen, J.S. Reparaz, A. Hoffmann, Excited state properties of donor bound excitons in ZnO, Phys. Rev. B 82 (2010) 115207.
[66] J. T-Thienprasert, S. Rujirawat, W. Klysubun, J.N. Duenow, T.J. Coutts, S.B. Zhang, D.C. Look, S. Limpijumnong, Compensation in Al-Doped ZnO by Al-Related Acceptor Complexes: Synchrotron X-Ray Absorption Spectroscopy and Theory, Phys. Rev. Lett. 110 (2013) 055502.
[67] D.O. Demchenko, B. Earles, H.Y. Liu, V. Avrutin, N. Izyumskaya, Ü. Özgür, H. Morkoç, Impurity complexes and conductivity of Ga-doped ZnO, Phys. Rev. B 84 (2011) 075201.
[68] R. Noriega, J. Rivnay, L. Goris, D. Kälblein, H. Klauk, K. Kern, L.M. Thompson, A.C. Palke, J.F. Stebbins, J.R. Jokisaari, G. Kusinski, A. Salleo, Probing the electrical properties of highly-doped Al:ZnO nanowire ensembles, J. Appl. Phys. 107 (2010) 074312.
[69] Y.K. Frodason, K.M. Johansen, T.S. Bjorheim, B.G. Svensson, A. Alkauskas, Zn vacancy-donor impurity complexes in ZnO, Phys. Rev. B, 97 (2018) 104109.
[70] J.L. Lyons, J.B. Varley, D. Steiauf, A. Janotti, C.G. Van de Walle, First-principles characterization of native-defect-related optical transitions in ZnO, J. Appl. Phys. 122 (2017) 035704.
[71] A. Escobedo-Morales, U. Pal, Defect annihilation and morphological improvement of hydrothermally grown ZnO nanorods by Ga doping, Appl. Phys. Lett. 93 (2008) 193120.
[72] A. Saenz-Trevizoa, P. Amezaga-Madrid, P. Piza-Ruiz, W. Antunez-Flores, M. Miki-Yoshida, Optical Band Gap Estimation of ZnO Nanorods, Mater. Res. Ibero Amer. J. Mater. 19 (2016) 33-38.
[73] J.D. Ye, S.L. Gu, S.M. Zhu, S.M. Liu, Y.D. Zheng, R. Zhang, Y. Shi, Fermi-level band filling and band-gap renormalization in Ga-doped ZnO, Appl. Phys. Lett. 86 (2005) 192111.
[74] C.S. Turchi, D.F. Ollis, Photocatalytic degradation of organic water contaminants: Mechanisms involving hydroxyl radical attack, J. Catal. 122 (1990) 178-192.
[75] M.A. Behnajady, N. Modirshahla, R. Hamzavi, Kinetic study on photocatalytic degradation of C.I. Acid Yellow 23 by ZnO photocatalyst, J. Hazard. Mater. 133 (2006) 226-232.

[76] S. Verma, B. Tirumala Rao, R. Singh, R. Kaul, Photocatalytic degradation kinetics of cationic and anionic dyes using Au–ZnO nanorods: Role of pH for selective and simultaneous degradation of binary dye mixtures, Ceram. Int. 47 (2021) 34751-34764.
[77] H. Wang, S. Baek, J. Song, J. Lee, S. Lim, Microstructural and optical characteristics of solution-grown Ga-doped ZnO nanorod arrays, Nanotechnol. 19 (2008) 075607.
[78] D. Pradhan, K.T. Leung, Vertical Growth of Two-Dimensional Zinc Oxide Nanostructures on ITO-Coated Glass: Effects of Deposition Temperature and Deposition Time, J. Phys. Chem. C 112 (2008) 1357-1364.
[79] J.H. Zheng, Q. Jiang, J.S. Lian, Synthesis and optical properties of flower-like ZnO nanorods by thermal evaporation method, Appl. Surf. Sci. 257 (2011) 5083-5087.
[80] E. McCafferty, J.P. Wightman, Determination of the concentration of surface hydroxyl groups on metal oxide films by a quantitative XPS method, Surf. Interface Anal. 26 (1998) 549-564.
[81] I. Gromyko, M. Krunks, T. Dedova, A. Katerski, D. Klauson, I. Oja Acik, Surface properties of sprayed and electrodeposited ZnO rod layers, Appl. Surf. Sci. 405 (2017) 521-528.
[82] M.Y. Guo, A.M.C. Ng, F. Liu, A.B. Djurišić, W.K. Chan, Photocatalytic activity of metal oxides—The role of holes and OH radicals, Appl. Catal.-B: Environ. 107 (2011) 150-157.
[83] M.Y. Guo, A.M.C. Ng, F. Liu, A.B. Djurišić, W.K. Chan, H. Su, K.S. Wong, Effect of Native Defects on Photocatalytic Properties of ZnO, J. Phys. Chem. C 115 (2011) 11095-11101.
[84] E.S. Jang, J.H. Won, S.J. Hwang, J.H. Choy, Fine Tuning of the Face Orientation of ZnO Crystals to Optimize Their Photocatalytic Activity, Adv. Mater. 18 (2006) 3309-3312.
[85] G.R. Li, T. Hu, G.L. Pan, T.Y. Yan, X.P. Gao, H.Y. Zhu, Morphology−Function Relationship of ZnO: Polar Planes, Oxygen Vacancies, and Activity, J. Phys. Chem. C 112 (2008) 11859-11864.
[86] A. McLaren, T. Valdes-Solis, G. Li, S.C. Tsang, Shape and Size Effects of ZnO Nanocrystals on Photocatalytic Activity, J. Am. Chem. Soc. 131 (2009) 12540-12541.
[87] Y. Liu, Z.H. Kang, Z.H. Chen, I. Shafiq, J.A. Zapien, I. Bello, W.J. Zhang, S.T. Lee, Synthesis, Characterization, and Photocatalytic Application of Different ZnO Nanostructures in Array Configurations, Cryst. Growth Des. 9 (2009) 3222-3227.
[88] N. Kislov, J. Lahiri, H. Verma, D.Y. Goswami, E. Stefanakos, M. Batzill, Photocatalytic Degradation of Methyl Orange over Single Crystalline ZnO: Orientation Dependence of Photoactivity and Photostability of ZnO, Langmuir 25 (2009) 3310-3315.
[89] X. Zhang, J. Qin, Y. Xue, P. Yu, B. Zhang, L. Wang, R. Liu, Effect of aspect ratio and surface defects on the photocatalytic activity of ZnO nanorods, Sci. Rep. 4 (2014) 4596.
[90] S.R. Morrison, T. Freund, Chemical Role of Holes and Electrons in ZnO Photocatalysis, J. Chem. Phys. 47 (1967) 1543-1551.
[91] C. Soci, A. Zhang, B. Xiang, S.A. Dayeh, D.P.R. Aplin, J. Park, X.Y. Bao, Y.H. Lo, D. Wang, ZnO nanowire UV photodetectors with high internal gain, Nano Lett. 7 (2007) 1003-1009.
[92] J. Yu, J. Low, W. Xiao, P. Zhou, M. Jaroniec, Enhanced Photocatalytic CO_2-Reduction Activity of Anatase TiO_2 by Coexposed {001} and {101} Facets, J. Am. Chem. Soc. 136 (2014) 8839-8842.